9 NMR and β-NMR Studies of Diffusion in Interface-Dominated and Disordered Solids

Paul Heitjans, Andreas Schirmer, and Sylvio Indris

9.1 Introduction

The topic of this chapter concerns diffusion studies via nuclear magnetic relaxation in solids with deviations from three-dimensional (3D) long-range order. These include, on the one hand, well-defined layer-crystalline materials with very large planar internal interfaces and, on the other hand, systems with highly complex internal interfaces as well as 3D amorphous solids where the structural disorder is of interest.

In layer-crystalline materials a strong anisotropy of the atomic or intermolecular coupling prevails. It often leads to the formation of atomic or molecular layers being weakly bonded in the direction perpendicular to the planes. As examples graphite and transition metal dichalcogenides will be considered. Between the layers of these materials, regarded as 'hosts', other atomic or molecular species may be built in as weakly bonded 'guests' which often are quite mobile. The corresponding process is called intercalation, its result is an intercalation compound [1–3]. These are quasi-2D solids with large internal interfaces. On the one hand, they are of technical interest; e. g., intercalation and deintercalation may in the case of an ionic guest be used as a charging and decharging cycle of a secondary battery component. On the other hand, intercalation materials show a large variety of structural and dynamical properties and may thus be used as model systems to study many phenomena in reduced dimensionality. Even with in-plane disorder, intercalation compounds show long-range ordered stacking of the layers with a fixed periodicity which is governed by the host material.

Another class of interface-dominated materials, which however are highly complex, are nanocrystalline materials [4,5]. They consist of crystalline grains of a diameter of typically 10 nm which is about three orders of magnitude below the respective value for normal poly-, i. e. microcrystalline materials. The nanometer-sized grains are surrounded by grain boundary regions with high defect concentration. These regions may form a network and share up to 50 % of the volume of the material. The mass density of the interfacial regions can be reduced to 80 % of the crystalline bulk. Nanocrystalline solids may thus be regarded as materials with inhomogeneously distributed free volume; they exhibit heterogeneous disorder. The density of interfaces is of the order of $10^9\,\mathrm{m}^2/\mathrm{m}^3$, similar to that of the planar interfaces in the intercalation

compounds. The nanocrystalline materials dealt with in this chapter are oxide and non-oxide ceramics. Nanocrystalline metals are briefly addressed in Chap. 8.

A third class of solid state systems considered here are amorphous materials, in particular ion conducting oxide glasses [6–8]. Contrary to nanocrystalline materials, these are homogeneously disordered with no internal interfaces. In this case free volume is homogeneously distributed. In general the density is reduced only by a few percent with respect to the ordered phase.

In order to disentangle the influences of disorder and low-dimensionality on the diffusional properties, the respective 3D ordered modifications should be studied in parallel as reference materials. In fact, besides the quasi-2D layered crystals the respective 3D modification, besides the nanocrystalline the normal coarse-grained material and besides the glass the respective crystal with identical chemical composition were investigated whenever possible.

As explained in Chap. 1, diffusion has aspects of both macroscopic material transport and microscopic jump processes. Correspondingly, macroscopic and microscopic experimental methods may be distinguished [9]. Nuclear magnetic resonance (NMR) techniques measuring spin relaxation, including beta-radiation detected NMR (β-NMR), which are dealt with in this chapter, belong to the latter. Macroscopic and microscopic techniques may further be classified as nuclear [10] and non-nuclear methods, respectively (cf. [9, 11]). Microscopic nuclear methods other than NMR relaxation spectroscopy are quasielastic neutron scattering (Chaps. 3 and 13) and Mößbauer spectroscopy (Chap. 2). They are capable to explore the jump geometry in addition to the jump rates. However, their dynamical ranges are more restricted [9]. An example for a microscopic non-nuclear technique is the measurement of the frequency-dependent ionic conductivity (Chap. 21).

An NMR technique probing macroscopic transport is field gradient NMR, which is treated in Chap. 10. Classical macroscopic nuclear and non-nuclear techniques are, respectively, the radiotracer technique (Chap. 1) and measurements of the d.c. ionic conductivity [12].

In the following we first recall the basic features of the influence of diffusion on NMR longitudinal relaxation (spin-lattice relaxation) and transverse relaxation (spin-spin relaxation), the latter being closely related to the NMR linewidth. We start from the ordinary case of 3D media and point out the deviations expected for two-dimensional and disordered systems (Sect. 9.2). Some principles of NMR techniques for measuring spin relaxation times of stable (Sect. 9.3) and β-radioactive probe nuclei (Sect. 9.4) are then presented. Finally experimental examples obtained by these methods in intercalation compounds (Sect. 9.5), nanocrystalline materials (Sect. 9.6) and glasses (Sect. 9.7) are reviewed.

9.2 Influence of Diffusion on NMR Spin-Lattice Relaxation and Linewidth

Diffusion can be probed by spin-lattice relaxation (SLR) caused by the temporal fluctuations of local fields due to the motion of particles carrying a nuclear spin. The principle can be understood from the simple picture of a probe spin precessing in an external magnetic field $\boldsymbol{B}_0$ with a Larmor precession frequency ω_L given by $\omega_\mathrm{L} = \gamma B_0$, where the magnetogyric ratio γ connects nuclear magnetic moment and angular momentum. The nuclear spin will be reversed, i. e. the transition probability will be maximum, when ω_L is in resonance with the frequency of a transverse alternating field $\boldsymbol{B}_1$. This may be an external radio-frequency field or the internal fluctuating field due to the motion of the atoms. In the following the latter case will be regarded more closely.

The fluctuating field which may be dipolar magnetic from neighbouring nuclei as well as quadrupolar electric from local electric field gradients can be described by the correlation function $G(t)$ which contains the temporal information on the atomic diffusion process [13–15]. The correlation time τ_c characterizing $G(t)$ is within a factor of the order of unity equal to the mean residence time τ between successive atomic jumps. Relevant for SLR is the spectral density function $J(\omega)$ of the fluctuating local field which is the Fourier transform of the correlation function $G(t)$ and extends up to frequencies of the order of τ_c^{-1}. Transitions between the energy levels of the spin system will be induced, i. e. spin-lattice relaxation becomes effective, when $J(\omega)$ has components at the transition frequencies. The spin-lattice relaxation rate T_1^{-1}, being a measure of the transition probability, is roughly given by

$$T_1^{-1} \propto J(\omega_\mathrm{L}) \quad . \tag{9.1}$$

Full expressions describing the relaxation due to dipolar interaction between like and unlike spins are given in (9.27) and (9.31), respectively, in the Appendix (Sect. 9.9)). The basic characteristics of T_1^{-1} in a 3D system with random jump diffusion can be derived from the simple exponential correlation function

$$G(t) = G(0) \cdot \exp(-|t|/\tau_\mathrm{c}) \tag{9.2}$$

assumed by Bloembergen, Purcell and Pound (BPP) [16]. The corresponding Lorentzian shaped spectral density function is given by

$$J(\omega) = G(0) \cdot \frac{2\tau_\mathrm{c}}{1 + (\omega\tau_\mathrm{c})^2} \quad . \tag{9.3}$$

The correlation time τ_c, like the mean residence time τ, will generally depend on temperature T according to the Arrhenius relation

$$\tau_\mathrm{c} = \tau_{\mathrm{c}0} \cdot \exp(E_\mathrm{A}/k_\mathrm{B}T) \quad , \tag{9.4}$$

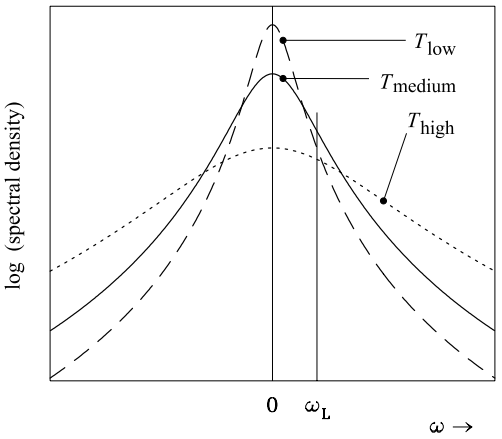

Fig. 9.1. Lorentzian spectral density function for different temperatures T. For a chosen value of the Larmor frequency ω_L the spectral density will be maximum for the medium T value where $\omega_L \tau_c \simeq 1$.

where E_A is the activation energy of the diffusion process. Fig. 9.1 shows $J(\omega)$ as an even function for three different temperatures taking into account that $\int J(\omega) d\omega$ is constant. It illustrates that $T_1^{-1}(T)$, measured at a certain Larmor frequency ω_L, passes through a maximum at a specific temperature which is determined by the condition $\omega_L \tau_c \approx 1$.

Quantitatively, the standard behaviour of T_1^{-1} in a 3D system is shown in Fig. 9.2 for the experimental example of self-diffusion in lithium [17] which was studied by β-NMR (Sect. 9.4). In the usual representation of $\log T_1^{-1}$ vs. $1/T$ the peak for each Larmor frequency (magnetic field) is symmetric. At temperatures above and below the maximum, which correspond to the limiting cases $\omega_L \tau_c \ll 1$ and $\omega_L \tau_c \gg 1$, respectively, the slopes yield the activation energy E_A. The SLR rate shows no ω_L dependence in the high-T limit and follows the power law $T_1^{-1} \propto \omega_L^{-2}$ in the low-T limit.

While Fig. 9.2 apparently reflects the main features of the BPP model predictions, the accuracy of the data enabled a comparison with a more refined model, namely the encounter model of correlated self-diffusion (cf. Chap. 3, Sect. 3.7) which, in fact, is represented by the continuous lines. There it has been taken into account that in the present case of β-NMR the ^{8}Li nuclei interact with unlike nuclei only (cf. (9.31) in the Appendix (Sect. 9.9)). From the fit τ_c values have been extracted over almost seven decades. Li has in fact been used as a test case for further diffusion-related NMR work and seems to be the best studied 3D ordered system concerning relaxation [18–23].

Much more pronounced deviations from the BPP model than in the case of the 3D encounter model are to be expected for low-dimensional and disordered systems being of interest here. The quantities bearing information spe-

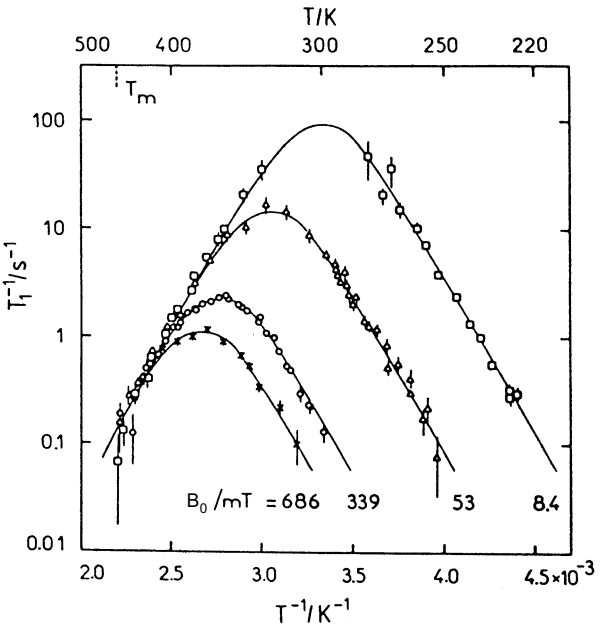

Fig. 9.2. Demonstration of the characteristic temperature and frequency dependence of the diffusion-induced SLR rate in 3D systems exemplified by ^{8}Li in polycrystalline Li. The B_0 values correspond to $\omega_L/2\pi = 4.32$ MHz, 2.14 MHz, 334 kHz and 53 kHz [17].

cific for the jump diffusion mechanism are the slopes of the high-T and low-T flanks of the $\log T_1^{-1}$ vs. $1/T$ plot. In Table 9.1 the corresponding predictions from simple models for low-dimensional diffusion [24, 25] are compared with the standard 3D behaviour. It is noted that dimensionality effects show up only in the high-T region where several jumps occur before one precession of the probe spin is completed ($\tau_c \ll \omega_L^{-1}$). The functional dependences are valid not only in the case of discrete jump vectors pertaining to ordered solids but also in the case of continuous diffusion. In the low-T region, however, the $\tau_c^{-1}\omega_L^{-2}$ dependence (cf. Fig. 9.2), which applies to the 1D through 3D cases, is true only for jump diffusion. In the case of continuum diffusion a $\tau_c^{-1/2}\omega_L^{-3/2}$ dependence is predicted, which is thus weaker in both variables than for jump diffusion.

SLR in disordered systems is not explicitly included in Table 9.1. However, continuum diffusion is discussed as bearing resemblance to diffusion in disordered solids due to varying distances of atomic sites. Indeed, the SLR rate in amorphous and defective crystalline materials has often been found to show an asymmetric $\log T_1^{-1}$ vs. $1/T$ peak with a smaller (absolute) slope on the low-T side and an ω_L dependence characterized by

Table 9.1. Asymptotic behaviour of $T_1^{-1}(\tau_c, \omega_L)$ for diffusion processes with different dimensionalities

	$\omega_L\tau_c \ll 1$ (high T)	$\omega_L\tau_c \gg 1$ (low T)	
		jump diffusion	continuum diffusion
3D	$\propto \tau_c$	$\propto \tau_c^{-1}\omega_L^{-2}$	$\propto \tau_c^{-1/2}\omega_L^{-3/2}$
2D	$\propto \tau_c \ln(1/\omega_L\tau_c)$		
1D	$\propto \tau_c(\omega_L\tau_c)^{-1/2}$		

$$T_1^{-1} \propto \omega_L^{-\alpha} \tag{9.5}$$

with $\alpha \leq 2$.

There are models for SLR in disordered ion conductors such as the assumption of distribution functions of jump correlation times [26], the counterion model [27], the coupling concept [28] and the jump relaxation model [29]. In Chaps. 20 and 21 up-to-date versions of the latter ones are presented mainly with respect to conductivity measurements. These models predict

$$T_1^{-1} \propto \omega_L^{-\alpha} \cdot \exp\left(-\frac{E_{NMR}^{lT}}{k_B T}\right) \tag{9.6}$$

with $1 < \alpha \leq 2$ on the low-T side. The corresponding activation energy E_{NMR}^{lT} should be related to E_{NMR}^{hT}, characterizing the slope on the high-T side, by

$$E_{NMR}^{lT} = (\alpha - 1) \cdot E_{NMR}^{hT} \quad . \tag{9.7}$$

Thus, in the frame of these models, the parameter α links the frequency dependence of T_1^{-1} to the asymmetry of the peak.

Monte Carlo simulation studies of the correlation functions in disordered ionic conductors ([30], see also Chap. 20) agree with these findings and show that the deviations from the BPP behaviour are the consequence of the combined effect of structural disorder and Coulomb interactions of the moving particles. Structural disorder is modelled in these simulations by using a percolation approach.

By means of the parameter α, SLR data may be related to data from other spectroscopic methods investigating, e. g., the dynamic conductivity or incoherent neutron scattering (cf. Chap. 20). Figs. 9.3 and 9.4 summarize the expected behaviour of the diffusion-induced SLR rate as a function of correlation time and frequency, respectively, for diffusion in an (ordered) 2D system and a (3D) disordered system in comparison with the BPP case.

If spin-lattice relaxation is not probed with reference to the static external field $\boldsymbol{B}_0$ but in a resonant alternating field $\boldsymbol{B}_1$ (see Sect. 9.3), the SLR rate in the rotating frame, $T_{1\rho}^{-1}$, is measured. It approximately obeys the relation

$$T_{1\rho}^{-1} \propto J(2\omega_1) \tag{9.8}$$

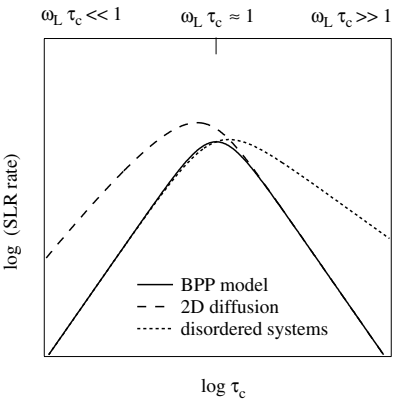

Fig. 9.3. Schematic representation of log (SLR rate) vs. log (correlation time) (corresponding to reciprocal temperature) for diffusion in the BPP case and the expected deviations for 2D systems and disordered systems.

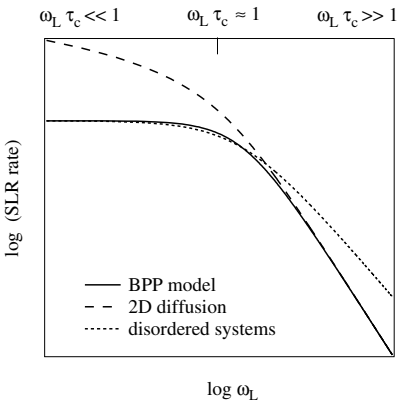

Fig. 9.4. Schematic representation of log (SLR rate) vs. log (Larmor frequency) (or magnetic field) for the BPP case and the expected deviations for 2D systems and disordered systems.

where $\omega_1 = \gamma B_1$. The full expression for the case of 3D diffusion is given in (9.30) in the Appendix (Sect. 9.9). Since $B_1 \ll B_0$, the condition $\omega_1 \tau_c \approx 0.5$ for the maximum of $T_{1\rho}^{-1}(T)$ entails that considerably longer correlation times are probed than by T_1^{-1} measurements.

Besides SLR measurements of T_1^{-1} and $T_{1\rho}^{-1}$ also measurements of the NMR linewidth, which is related to the spin-spin relaxation time T_2, can give information about microscopic parameters of diffusion. In general, nuclear spins in an external magnetic field B_0 experiencing dipolar interaction in a homogeneous solid at low temperatures show one broad static NMR line without substructure. This is because the nuclei under investigation are located at sites with different spin environments resulting in different local magnetic fields superimposed on the external magnetic field B_0. In this way many contributions with different resonance frequencies form a broad NMR line with a width of some kHz. This is the rigid lattice linewidth $\Delta\nu_{\mathrm{R}}$ which corresponds to the spin-spin relaxation rate T_2^{-1} at low temperatures. When the sample is heated the ions start moving through the solid. The temperature dependence of the jump rate τ^{-1} is given by an Arrhenius relation analogous to that of the correlation rate τ_{c}^{-1} (cf. (9.4)).

At higher temperatures the hopping of the ions becomes so fast that they are experiencing the same average local field. This sets in when the correlation rate becomes larger than the width of the rigid lattice line, i. e.

$$\tau_{\mathrm{c}}^{-1} \gtrsim 2\pi \cdot \Delta\nu_{\mathrm{R}} \quad . \tag{9.9}$$

Then all nuclei have the same resonance frequency and a narrowed NMR line is observed. This phenomenon is called motional narrowing. In this temperature regime the spin-spin relaxation rate is approximately given by

$$T_2^{-1} \propto J(0) \propto \tau_c \quad . \tag{9.10}$$

The functional dependence of the linewidth on temperature allows one to determine τ_{c0} and E_A.

The situation when at even higher temperatures the correlation rate exceeds the Larmor frequency,

$$\tau_c^{-1} > \omega_L \quad , \tag{9.11}$$

is called extreme motional narrowing. The full expression for the spin-spin relaxation rate in the motional narrowing and the extreme motional narrowing regime for 3D diffusion is given in (9.28) in the Appendix (Sect. 9.9). Then the spin-spin relaxation rate T_2^{-1} and the spin-lattice relaxation rates T_1^{-1} and $T_{1\rho}^{-1}$ should all have the same value, and the residual NMR linewidth is determined by the inhomogeneity of the magnetic field.

Additional contributions to the lineshape can occur for nuclei with spin $I \geq 1$. These have a quadrupolar moment which interacts with electric field gradients, when present due to low crystal symmetry at the site of the nuclei.

The general features of the relaxation rates T_1^{-1}, $T_{1\rho}^{-1}$ and T_2^{-1} in the standard case of 3D diffusion via random jumps are summarized in Fig. 9.5. The rates are plotted here as a function of $\omega_L \tau_c$ so that it can readily be seen that the T_1^{-1} maximum occurs for $\omega_L \tau_c \approx 1$. As mentioned above, the maximum of $T_{1\rho}^{-1}$ shows up for $\omega_1 \tau_c \approx 0.5$ and the constant value for T_2^{-1} is reached when $2\pi\,\Delta\nu_R \approx 1$. In the plot we used $\omega_L : \omega_1 : 2\pi\,\Delta\nu_R = 10^4 : 20 : 1$.

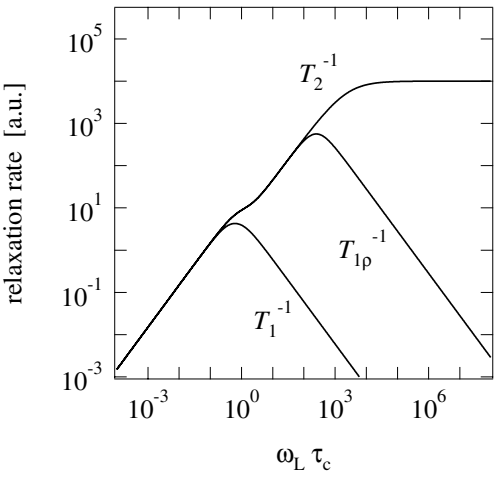

Fig. 9.5. Schematic representation of the relaxation rates T_1^{-1}, $T_{1\rho}^{-1}$ and T_2^{-1} vs. $\omega_L \tau_c$ for 3D diffusion via random jumps.

$\Delta\nu_{\mathrm{R}}$ is typically some tens kHz. The shoulder in the curves of $T_{1\rho}^{-1}$ and T_2^{-1} is due to contributions by the spectral densities at ω_{L} and $2\omega_{\mathrm{L}}$ in addition to those at $2\omega_1$ and $\omega = 0$, respectively (see (9.30) and (9.28)).

Concluding this section, we note that besides the description of diffusion induced NMR relaxation in the perturbation approach by spectral density functions, sketched here in a qualitative way, there are stochastic models. These yield a more general access to spin relaxation being not confined to the motional narrowing regimes (see, e. g., [31, 32] and references therein).

9.3 Basics of NMR Relaxation Techniques

Solid-state NMR, being based on the Boltzmann polarization of stable nuclei, is a very broad field and for a comprehensive treatment the reader is referred to various monographs [13, 14, 33–35]. Furthermore, detailed descriptions of NMR relaxation techniques are available (e. g. [36, 37]), and corresponding pulse programs are nowadays implemented in standard NMR spectrometers. We here confine ourselves to a brief outline of the basic principles of the measurements of longitudinal and transverse, i. e. spin-lattice and spin-spin relaxation times, respectively. A T_1 or T_2 measurement proceeds in two steps in the time domain:
(i) tilting the nuclear magnetization

$$\boldsymbol{M}_0 = N \cdot \frac{\gamma^2 \hbar^2 I(I+1)}{3k_{\mathrm{B}}T} \cdot \boldsymbol{B}_0 \tag{9.12}$$

of an ensemble of nuclei (number density N, spin I) at equilibrium in a static magnetic field $\boldsymbol{B}_0$ at temperature T by a pulsed alternating field.
(ii) detection of the magnetization $\boldsymbol{M}(t)$ as it relaxes back to $\boldsymbol{M}_0$.

The experimental set-up consists of the sample placed in a strong magnetic field $\boldsymbol{B}_0$ (of the order of some Tesla) in the z-direction and a coil wound around the sample for application of a perpendicular alternating field $\boldsymbol{B}_1(t)$ with frequency $\omega/2\pi$ in the radio-frequency (rf) regime. In this arrangement an equilibrium magnetization $\boldsymbol{M}_0$ is built up in the z-direction due to the Boltzmann population of the Zeeman energy levels (Fig. 9.6), which is given by (9.12).

The effect of simple rf-pulse sequences is discussed in the classical picture of a magnetization $\boldsymbol{M}$ moving in an external magnetic field. The equation of motion is [14]

$$\frac{\mathrm{d}\boldsymbol{M}}{\mathrm{d}t} = \boldsymbol{M} \times \gamma \left[\boldsymbol{B}_0 + \boldsymbol{B}_1(t)\right] \quad . \tag{9.13}$$

For discussion of the motion in an alternating magnetic field applied in the x-direction ($\boldsymbol{B}_1(t) = B_{x0}\cos(\omega t)\boldsymbol{e}_x$), time dependences are eliminated by using a coordinate system rotating about the $\boldsymbol{B}_0$ direction with angular velocity ω. Its axes are denoted in the following with x', y' and z', see Fig. 9.7. In such

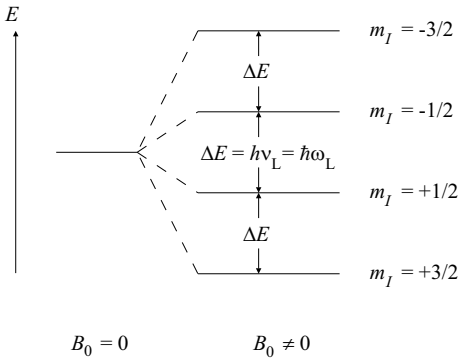

Fig. 9.6. Zeeman splitting of the nuclear energy level due to interaction of the nuclear spins with a static external field $\boldsymbol{B}_0$, here shown exemplarily for spin $I = 3/2$, $\gamma > 0$.

a system the effective magnetic field $\boldsymbol{B}_{\text{eff}}$ is composed of the static field $\boldsymbol{B}_0$, the alternating field $\boldsymbol{B}_1$ and a term $\boldsymbol{\omega}/\gamma$ which results from the transition to an accelerated reference frame (see Fig 9.8 (a)). When the x'-axis is chosen along $\boldsymbol{B}_1$ the equation of motion can be rewritten as

$$\frac{\mathrm{d}\boldsymbol{M}}{\mathrm{d}t} = \boldsymbol{M} \times \gamma \left[\left(B_0 - \frac{\omega}{\gamma} \right) \boldsymbol{e}_{z'} + B_1 \boldsymbol{e}_{x'} \right] = \boldsymbol{M} \times \gamma \boldsymbol{B}_{\text{eff}} \tag{9.14}$$

which means that the magnetization behaves as if it experienced a stationary magnetic field $\boldsymbol{B}_{\text{eff}}$. If the resonance condition $\omega = \omega_{\text{L}} = \gamma B_0$ is fulfilled for the alternating $\boldsymbol{B}_1$ field, the z' component of $\boldsymbol{B}_{\text{eff}}$ vanishes and the effective field is $B_1 \boldsymbol{e}_{x'}$ and $\boldsymbol{M}$ will rotate in the $z'-y'$ plane with a frequency $\omega_1 = \gamma B_1$ (see Fig. 9.8). The application of an alternating $\boldsymbol{B}_1$ with the duration t_{p} will result in a flipping of $\boldsymbol{M}$ to the angle $\theta_{\text{p}} = \gamma B_1 t_{\text{p}}$. In the laboratory reference frame this results in a nutational motion as shown in Fig. 9.9. By proper choice of t_{p}, $\boldsymbol{M}$ can be inverted ($\theta_{\text{p}} = \pi$) or tilted into the $x - y$ plane ($\theta_{\text{p}} = \pi/2$), where it will precess (in the laboratory reference frame) and induce an observable voltage in the coil. This is the free induction decay (FID).

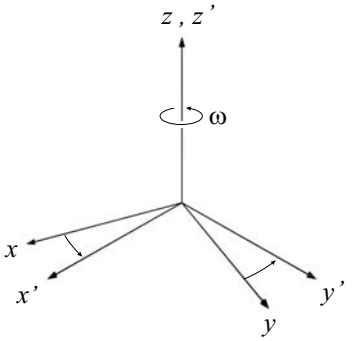

Fig. 9.7. The rotating reference frame rotating about the direction of the external magnetic field (z axis) with angular velocity ω.

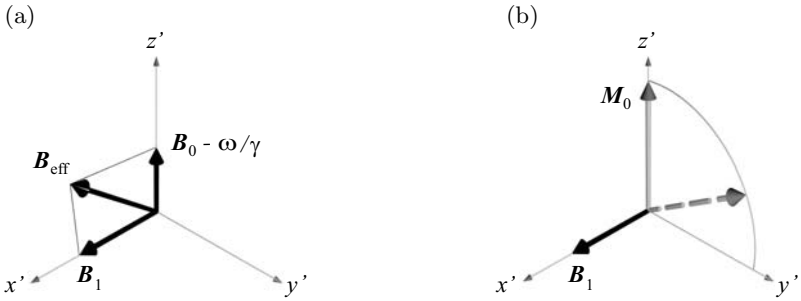

Fig. 9.8. (a) The effective magnetic field in the rotating reference frame. (b) The motion of the magnetization in the rotating reference frame for $\omega = \omega_{\mathrm{L}}$.

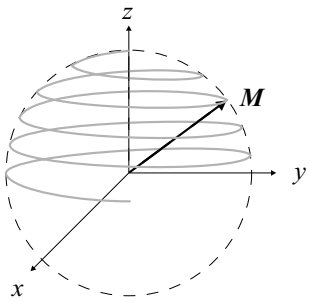

Fig. 9.9. Nutational motion of the magnetization in the laboratory reference frame due to an alternating magnetic field perpendicular to the static external field which is applied along the z axis.

After the π or $\pi/2$ pulse $\boldsymbol{M}$ will relax towards its equilibrium value M_0 along the $+z$-direction in the laboratory reference frame. The instantaneous M_z value may be described by

$$\frac{\mathrm{d}M_z}{\mathrm{d}t} = \frac{M_0 - M_z}{T_1} \tag{9.15}$$

with T_1 being the longitudinal or spin-lattice relaxation time. Equation (9.15) yields

$$M_z(t) = M_0[1 - A_{\mathrm{p}} \exp(-t/T_1)] \tag{9.16}$$

with $A_{\mathrm{p}} = 2$ (1) for an initial π pulse ($\pi/2$ pulse). $M_z(t)$ is monitored by the amplitude of the FID after a $\pi/2$ reading pulse at the evolution time τ_{e} which is varied.

In case that the magnetization $\boldsymbol{M}$ is not aligned parallel to the external magnetic field $\boldsymbol{B}_0$ the magnetization will precess around the magnetic field. Furthermore, the transverse components $M_{x'}$ and $M_{y'}$ will decay due to a dephasing of the nuclear spins which are in phase only directly after the rf pulse. The equilibrium values of $M_{x'}$ and $M_{y'}$ are zero. The magnitudes of $M_{x'}$ and $M_{y'}$ obey the equations

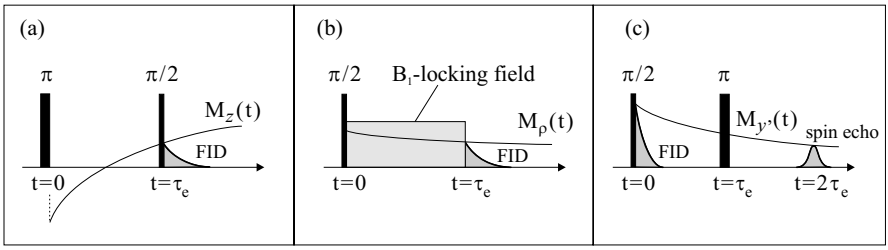

Fig. 9.10. (a) Principle of a T_1 measurement with the inversion-recovery pulse sequence $(\pi - \tau_e - \pi/2)$: After inversion and evolution time τ_e the magnetization $M(\tau_e)$ is probed with the $\pi/2$ pulse. (b) Principle of a $T_{1\rho}$ measurement: After a $\pi/2$ pulse $M_\rho(t)$ is locked by a $\pi/2$ phase shifted B_1-locking field and decays according to $M_\rho(t) = M_\rho(0)\exp(-t/T_{1\rho})$ which is probed at $t = \tau_e$ after switching off the locking field. (c) Principle of a T_2 measurement with a spin echo pulse sequence $(\pi/2 - \tau_e - \pi)$: After a $\pi/2$ pulse has turned the magnetization to the plane perpendicular to the external magnetic field it starts precessing around this field and its transverse component decays due to dephasing of the nuclear spins according to $M_{y'}(t) = M_0\exp(-t/T_2)$. The π pulse at time τ_e causes a refocussing of the spins at time $2\tau_e$ resulting in a spin echo signal. Its amplitude can be used to probe the magnetization $M_{y'}(2\tau_e)$.

$$\frac{\mathrm{d}M_{x'}}{\mathrm{d}t} = -\frac{M_{x'}}{T_2}$$
$$\frac{\mathrm{d}M_{y'}}{\mathrm{d}t} = -\frac{M_{y'}}{T_2} \tag{9.17}$$

with T_2 being the transverse or spin-spin relaxation time. After an initial $\pi/2$ pulse has turned the magnetization to the y direction, (9.17) yields

$$M_{y'}(t) = M_0\exp(-t/T_2) \quad . \tag{9.18}$$

In NMR spectrometers the coil around the sample is used for both steps of the experiment, irradiation of the rf pulse and detection of the signal response, i. e. the voltage induced by the precessing magnetization. Modern NMR spectrometers further supply rf pulses which are coherent with the possibility to control and switch the phase of different pulses. A widely used pulse sequence for measurements of the longitudinal relaxation time is illustrated in Fig. 9.10 (a). It should be noted that for T_1 measurements longer and more complex pulse sequences may be tailored to overcome limitations of the simple sequences. The latter suffer, e. g., from the dead time of the detection system after the strong rf pulse; in this case echo sequences may be used to shift the FID away from the rf pulse.

As an example of how phase and power switching with modern NMR spectrometers are used to extend the effective magnetic field range for spin-lattice relaxation measurements, the pulse sequence for spin locking and longitudinal relaxation in the rotating frame is shown in Fig. 9.10 (b). With a $\pi/2$

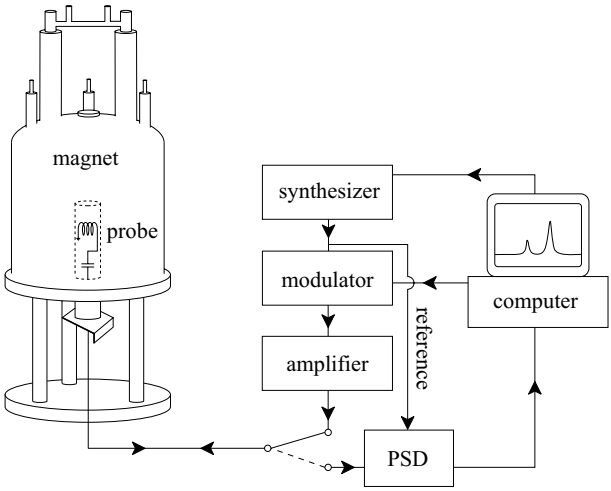

Fig. 9.11. Typical setup of an NMR spectrometer.

pulse the magnetization M_z is turned into the $x-y$ plane and locked parallel to $\boldsymbol{B}_1$ in a frame rotating about $\boldsymbol{B}_0$ with $\omega_\mathrm{L} = \gamma B_0$. During application of the $\boldsymbol{B}_1$ locking field the magnetization M_ρ in the rotating frame relaxes and $M_\rho(\tau_\mathrm{e})$ can be measured by monitoring the FID at the end of the pulse. Thus the relaxation time $T_{1\rho}$ is obtained. It reflects the spin relaxation in the locking field being typically some 10^{-4} T. Variation of the locking field amplitude gives access to studies of the field dependence of $T_{1\rho}$. Corresponding to the change in frequencies from the MHz to the kHz regime when SLR times in the rotating instead of the laboratory frame are measured, considerably longer motional correlation times can be studied. We note, that a technique to measure SLR times also in the laboratory frame at frequencies down to the kHz regime is field-cycling relaxometry [38], which, however, will not be discussed here.

Fig. 9.10 (c) shows a spin echo pulse sequence which can be used to probe the decay of the transverse magnetization component $M_{y'}$ and thus to measure the transverse relaxation time T_2. A $\pi/2$ pulse turns the magnetization to the plane perpendicular to the external magnetic field where it starts precessing around this field. Its transverse component which is built by the sum of the nuclear spins starts to decay because of a dephasing of the spins. The π pulse at time τ_e causes a refocussing of the spin system resulting in a so-called spin echo signal at time $2\tau_\mathrm{e}$. Its height is proportional to the magnetization $M_{y'}(2\tau_\mathrm{e})$ which is measured for different evolution times τ_e between the two pulses. According to (9.18) measurements with different delay times τ_e allow one to probe the decay of the transverse components and thus to determine T_2.

It is obvious from the discussion above that the basis of modern NMR techniques is data acquisition after pulsed excitation and subsequent Fourier transformation. The main components of a Fourier-NMR spectrometer are shown in Fig. 9.11. The sample is located in the coil of a rf resonant circuit which is part of the probe. This is located in the center of a superconductive magnet. The nuclei in the sample are excited by rf pulses which are generated, starting from a highly precise synthesizer, with a rf modulator and a high-power amplifier. The response signal of the sample nuclei, being weaker by many orders of magnitude, is directed via a rf switch to a phase sensitive detector (PSD), whose reference signal is provided by the synthesizer. The whole procedure which may include not only single pulses but complex pulse sequences, as described above, is controlled by a computer.

9.4 Method of β-Radiation Detected NMR Relaxation

Technical improvements have made NMR relaxation techniques described in Sect. 9.3 a tool of steadily increasing versatility. On the one hand, higher magnetic fields have improved the signal-to-noise ratio by increasing the Boltzmann factor. On the other hand, by using more sensitive amplifiers and digitized signal recorders weaker signals can be measured and less sample material or smaller samples under extreme conditions (e. g. high-pressure cells) can be used. An alternative approach is to replace the steps of the NMR relaxation experiments by unconventional ones which avoid certain limitations. In this section concepts of such a method, known as β-radiation detected NMR (β-NMR [39]) relaxation, will be introduced and discussed.

The principle of β-NMR relaxation is the use of the β-decay radiation asymmetry of polarized, short-lived β-emitters embedded in the solid in order to monitor the nuclear polarization and its decrease due to longitudinal, i. e. spin-lattice relaxation [11]. The two steps of the classical NMR relaxation experiment (Sect. 9.3) are replaced by (i) on-line production of the short-lived polarized probe nuclei with lifetimes τ_β ranging from some 10 ms to some 100 s, and (ii) in-situ measurement of the β-asymmetry during a subsequent time interval of a few lifetimes. The signal amplitude resulting from step (i) is determined by the angular distribution of the emission probability $W(\theta)$ of β-particles from an ensemble of polarized β-active nuclei into a solid angle element at angle θ between polarization and emission direction

$$W(\theta) = 1 + f \cdot \frac{v}{c} \cdot A \cdot \cos\theta \quad . \tag{9.19}$$

f is the dipolar polarization characterized by a linearly varying population of the nuclear Zeeman levels, v is the electron velocity, c the velocity of light and A is a constant for the specific β-decay. The β-decay radiation asymmetry a_β is given by the 0°-180°-difference of $W(\theta)$ and is a direct measure of

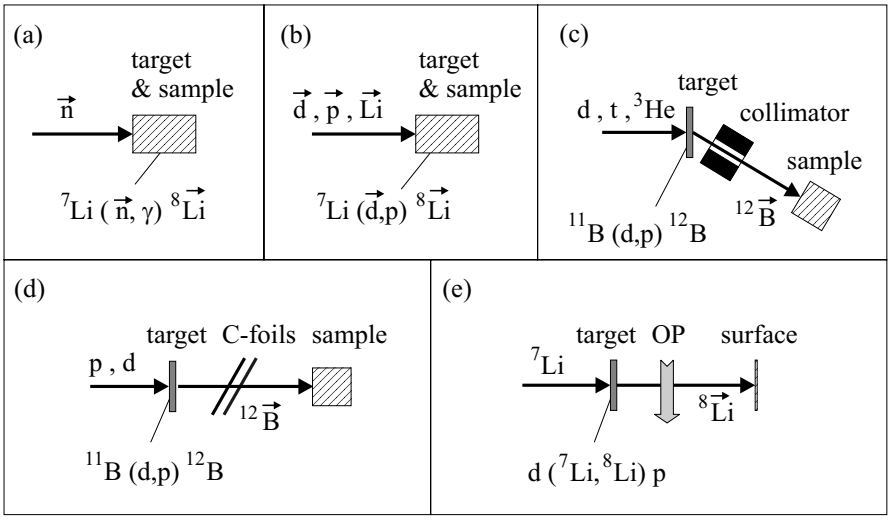

Fig. 9.12. Different techniques to produce polarized β-active nuclei in condensed matter: (a) capture of polarized neutrons, (b) nuclear reaction with polarized accelerated particles, (c) particle reaction with selected recoil angle, (d) nuclear reaction with beam-foil polarization, (e) particle reaction and polarization by optical pumping (OP). In each case an exemplary nuclear reaction is given.

$P = f\frac{v}{c}A$, the experimentally accessible polarization. It reflects the dipolar polarization f and any changes of it.

Variants of the β-NMR method can be classified according to the way the short-lived β-emitters embedded in the sample are generated and polarized, which may be done in one or two steps. The polarized β-emitters can be produced on-line in nuclear reactions with polarized reactor neutrons or with accelerator ions [39, 40]. Schemes of various production routes are shown in Fig. 9.12. The generation and polarization by capture of polarized thermal or cold neutrons (Fig. 9.12 (a)) will be dealt with in some detail below. With accelerators different techniques may be applied (Fig. 9.12 (b)-(e)). First, polarized incident particles may be used again (Fig. 9.12 (b)). In this case one can profit from a sufficiently high polarization transfer to the short-lived β-emitters in reactions of the type ^{7}Li($\vec{d}$,p)$^{8}\vec{Li}$ or ^{16}O($\vec{d}$,n)$^{17}\vec{F}$ [39]. The accelerator ions have typically to have energies above 1 MeV. The β-emitters, which can be β^{+} as well as β^{-}-emitters, have kinetic recoil energies in the range of several keV and are stopped in the sample.

With unpolarized accelerator ions (Fig. 9.12 (c)-(e)) the short-lived β-emitters emerging as recoil nuclei from the target foil have to be polarized prior to implantation into the sample. This can be achieved either by a proper selection of the recoil angle, into which the β-emitters escape from the reaction (Fig. 9.12 (c)), or by polarizing the short-lived β-emitters after the reac-

tion (Figs. 9.12 (d) and (e)). In the former case, the recoil angle selection of the short-lived β-emitters corresponds to an angular momentum selection with a polarization perpendicular to the reaction plane which is given by the trajectories of the accelerator ion and the recoil nuclei [39,41]. Another technique to obtain polarized β-emitters with unpolarized accelerator ions hitting the target is the use of hyperfine effects by passage of the β-emitters through carbon foils which are tilted with respect to the beam direction [42,43] (Fig. 9.12 (d)). A more established technique to polarize the recoil nuclei is optical pumping which in combination with mass-separator extraction offers access to a large variety of probe nuclei [44, 45] (Fig. 9.12 (e)).

In all these nuclear techniques the polarization P, which in the classical NMR experiments is determined by a Boltzmann factor and which gives rise to a macroscopic magnetization M_0 (cf. (9.12)), is larger by many orders of magnitude than a usual Boltzmann polarization and reaches some per cent.

Among the various β-NMR techniques sketched above, diffusion studies have essentially been performed with β-NMR after capture of polarized neutrons (Fig. 9.12 (a)) and after a particle reaction with selected recoil angle (Fig. 9.12 (c)). In the latter case the investigations were confined to bulk metals and semiconductors [46–50] which is beyond the scope of this chapter. Only very few diffusion studies were done using the optical pumping technique (Fig. 9.12 (e)), e. g. ^{8}Li surface diffusion on Ru(001) [51] and on Si(111) [52].

In the following the β-NMR technique after capture of polarized neutrons will be further outlined [53]. The sample abundantly containing the nuclei for the production reaction is placed in the field $\boldsymbol{B}_0$ of an electromagnet and irradiated with polarized cold neutrons. For example, in the case of the probe nucleus ^{8}Li the reaction is

$$\overrightarrow{\mathrm{n}} + {}^7\mathrm{Li} \longrightarrow {}^8\overrightarrow{\mathrm{Li}}^{*} \xrightarrow{\gamma's} {}^8\overrightarrow{\mathrm{Li}} \xrightarrow{\beta^-} 2\alpha\,.$$

Established probe nuclei available with the neutron capture technique are: ^{8}Li (τ_β = 1.2 s), ^{12}B (29 ms), ^{20}F (16 s), ^{23}Ne (57 s), ^{28}Al (3.2 min), ^{108}Ag (3.5 min), ^{110}Ag (35 s), ^{116}In (20 s).

Special features of the β-NMR method with respect to relaxation measurements are as follows. As outlined above, the polarization P is high and independent of a Boltzmann factor. Thus low values of the magnetic field (which provides the quantization axis) and high temperatures are accessible. The magnetic field has to be stronger than parasitic internal and external fields. The concentration of the probe nuclei is extremely small (typically 1 in 10^{18} other nuclei) and as a consequence spin diffusion, i. e. the polarization transfer by resonant mutual spin flips of like nuclei, is suppressed due to their large distance. Thus SLR by distant paramagnetic impurities, generally effective via spin diffusion in classical NMR relaxation measurements, does not contribute to β-NMR relaxation. The highly diluted probe nuclei

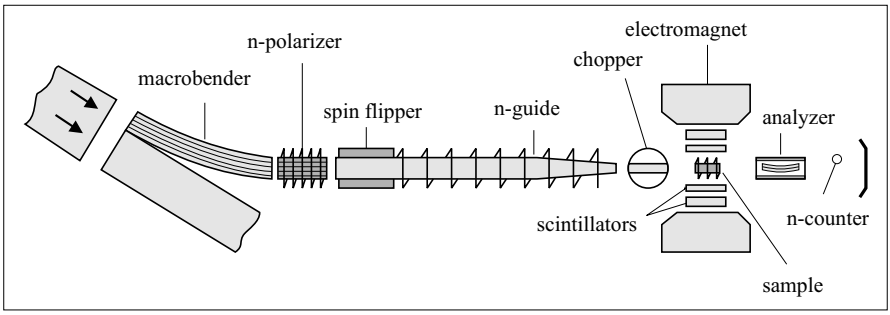

Fig. 9.13. Experimental set-up of the β-NMR spectrometer at the reactor FRJ-2 of the Forschungszentrum Jülich.

relax individually and the β-asymmetry signal stems from an inhomogeneous polarization average of the probe nuclei.

A technical advantage of β-radiation detected SLR is that no rf irradiation is required. The field B_0, correspondingly the Larmor frequency of the measurement, is easily variable and skin effect problems do not arise. Bulk metallic samples and/or metallic sample containers can be used. The latter is often desirable when corrosive materials are to be studied. The measurement of SLR times T_1 is restricted to a time window of at most $0.01\tau_\beta < T_1 < 100\tau_\beta$.

Fig. 9.13 shows the scheme of the β-NMR spectrometer at the research reactor of the Forschungszentrum Jülich [53]. The set-up consists of a neutron beam section with macrobender, neutron-polarizer and spin-flipper for branching-off, polarizing and polarization switching of cold neutrons with a broad wavelength distribution. The polarization switching is used in order to cancel instrumental asymmetries of the NMR apparatus. Its main components are chopper, collimator, sample in oven or cryostat, β-scintillator telescope detectors and electromagnet. The chopper is used for the separation of the production and the relaxation measurement periods of the short-lived nuclei. The β-scintillator telescopes are mounted on the pole faces 'North' and 'South' and register the counting rates Z_N and Z_S at $\theta = 0°$ and 180°, respectively, which yield the experimental β-asymmetry

$$a_\beta = \frac{Z_\mathrm{N} - Z_\mathrm{S}}{Z_\mathrm{N} + Z_\mathrm{S}} \quad . \tag{9.20}$$

As pointed out above, a_β is proportional to the nuclear polarization P. β-NMR relaxation measurements are performed by monitoring transients $a_\beta(t)$ after neutron activation pulses produced by the chopper. In simple cases monoexponential transients

$$a_\beta(t) = a_{\beta 0} \cdot \exp(-t/T_1) \tag{9.21}$$

with the SLR time T_1 are observed.

The NMR apparatus is further equipped with an rf source and a coil around the sample for recording resonance signals. In this mode the β-asymmetry is monitored under quasi-continuous neutron-activation conditions while an rf field, scanning a frequency range in the vicinity of the Larmor frequency, is irradiated on the sample. Neutron flux and polarization can be controlled with a counter and an analyser.

9.5 Intercalation Compounds

In the introduction to this chapter (Sect. 9.1) the role of a prototype 2D material for understanding both, diffusion mechanisms and material modifications, has been mentioned. Due to its simple structure and amphoteric character, graphite as host material for intercalation has attracted much interest for structural [2] and dynamic [3] studies. Graphite can be intercalated with electron donors like alkali metals or with electron acceptors like Br or more complex molecules (as for example HNO_3, AsF_5). Other prototype host materials with 2D internal interfaces are transition metal dichalcogenides [54]. Similar to the case of graphite, Li-intercalated TiS_2 as a model system for translational diffusion was investigated.

9.5.1 Lithium Graphite Intercalation Compounds

Lithium can easily be intercalated into graphite to form the stage-1 compound LiC_6, i. e. to attain a stacking of alternating C and Li layers. The number of subsequent host layers of an intercalation compound, here the graphite sheets, denotes the stage of the compound. The Li layers in LiC_6 form a commensurate $(\sqrt{3} \times \sqrt{3})\ R30°$ superstructure as shown in Fig. 9.14. The stage-2 compound LiC_{12} has the same structure of the Li planes, which are separated by two C layers.

SLR of ^{8}Li in both stages was investigated with the β-NMR method. The samples were made from highly oriented pyrolytic graphite (HOPG). The

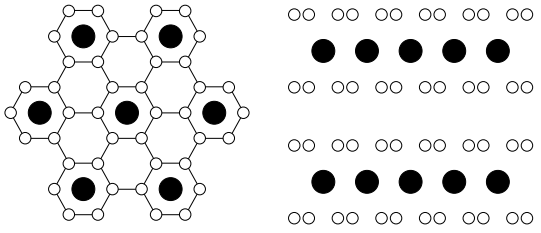

Fig. 9.14. Structure of Li graphite intercalation compounds. Left: View upon the in-plane structure of LiC_6 and LiC_{12}. Li atoms (full circles) are located above the hexagons of C atoms (open circles). Right: View upon a plane containing the $\boldsymbol{c}$ axis of LiC_{12}

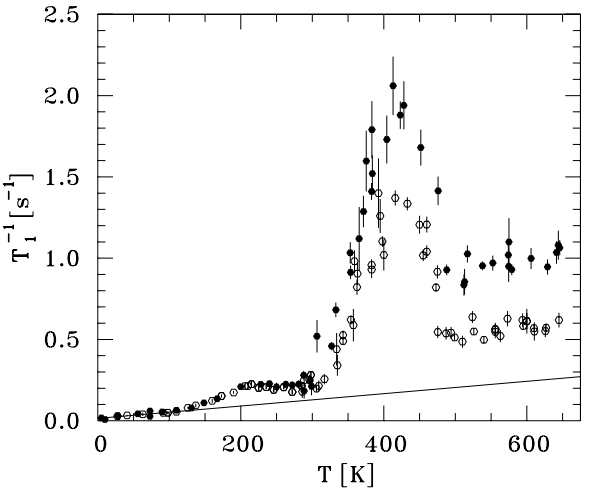

Fig. 9.15. T dependence of the SLR rate of ^{8}Li in the stage-2 graphite intercalation compound LiC_{12} for $B_0 = 37\,\mathrm{mT}$ and two orientations of $\boldsymbol{B}_0$ with respect to the $\boldsymbol{c}$ axis ($\boldsymbol{B}_0 \parallel \boldsymbol{c}$: open dots, $\boldsymbol{B}_0 \perp \boldsymbol{c}$: full dots). The straight line represents the SLR rate contribution due to coupling to conduction electrons [59].

graphite sheets in HOPG are stacked in a single-crystalline manner in the $\boldsymbol{c}$ direction. In the crystallographic $(\boldsymbol{a}, \boldsymbol{b})$ plane the C layers are oriented at random.

Fig. 9.15 gives an overview of T_1^{-1} measured as a function of T at a constant value of B_0 for the orientations $\boldsymbol{B}_0 \parallel \boldsymbol{c}$ and $\boldsymbol{B}_0 \perp \boldsymbol{c}$. As another important parameter, the value of B_0 was varied between 10 mT and 400 mT. This corresponds to an $\omega_\mathrm{L}/2\pi$ range from 0.06 MHz to 2.5 MHz which is hardly accessible with conventional NMR techniques. The temperature dependence of T_1^{-1} shows different regions. Here we only touch upon the temperature region below 100 K and concentrate on the range between 300 K and 500 K, where a pronounced T_1^{-1} peak shows up.

For $T < 100\,\mathrm{K}$, T_1^{-1} increases linearly with T and does neither depend on orientation nor on magnitude of $\boldsymbol{B}_0$. This is a feature of SLR due to coupling to conduction electrons. A detailed representation of the data and a discussion of the implications on the electronic properties of LiC_{12} is given in [55]. This SLR mechanism persists also at higher temperatures and contributes as a background to the experimental T_1^{-1} values.

Between 300 K and 500 K, SLR is dominated by long-range Li motion [56] and the rate $T_{1\mathrm{d}}^{-1}$, obtained by subtracting the contribution due to conduction electrons from T_1^{-1}, exhibits a temperature dependence qualitatively similar to that depicted in Fig. 9.2. However, B_0 dependences of $T_{1\mathrm{d}}^{-1}$ were found on the low-T and high-T flanks of the diffusion-induced peak which can be characterized by

$$T_{1\mathrm{d}}^{-1} \propto B_0^{-\alpha} \text{ with } \begin{cases} \alpha \simeq 1.2 & \text{for low } T \ (\omega_\mathrm{L}\tau_\mathrm{c} \gg 1) \\ \alpha \simeq 0.4 \ldots 0.7 & \text{for high } T \ (\omega_\mathrm{L}\tau_\mathrm{c} \ll 1) \ . \end{cases}$$

On the low-T side, the value for α is smaller than expected for jump diffusion in ordered systems ($\alpha = 2$; cf. Table 9.1). It is close to that for continuum diffusion ($\alpha = 1.5$) and compatible with B_0 dependences observed in disordered systems with highly correlated ionic motion. On the high-T side, the observation of a B_0 dependence ($\alpha \neq 0$) indicates that SLR is governed by a low-D diffusion process. For a direct comparison with the asymptotic laws for 1D and 2D diffusion given in Table 1, however, one has to take into account that above 500 K T_1^{-1} does not reduce to the conduction electron contribution. This implies an additional contribution to T_1^{-1} which is weakly T dependent (partly reflected by the above spread of α values). After correction for this contribution the SLR data are compatible with a logarithmic B_0 dependence as predicted for 2D diffusion.

From the slope of the $\log T_{1\mathrm{d}}^{-1}$ vs. $1/T$ on the low-T side of the peak an activation energy of about 1 eV was estimated [56].

Analogous measurements on the stage-1 compound LiC_6 [57], where similar conclusions from the B_0 dependence of the SLR rate were drawn, yielded an activation energy of about 0.6 eV. Thus an additional C sheet between the Li layers seems to slow down the Li diffusion. This trend was also found in a lattice simulation calculation [58].

It is noted that the dependence of the SLR rate on orientation of the layer stacking $\boldsymbol{c}$ axis with respect to $\boldsymbol{B}_0$, not further discussed here, gives information on the type of interaction dominating SLR [57]. For a comparison of the β-NMR results with those from quasielastic neutron scattering on the same samples we refer to [59] and to Chap. 3, Sect. 3.11.

9.5.2 Lithium Titanium Disulfide – Hexagonal Versus Cubic

In the previous subsection diffusion-induced SLR in quasi-2D Li graphite intercalation compounds of different compositions (stages) with identical in-plane structures were studied. We now compare a layered (2D) Li dichalcogenide with a cubic 3D one having the same chemical composition.

The host material TiS_2, in its hexagonal modification (h-TiS_2), consists of two hexagonal closed packed S layers between which the Ti atoms occupy octahedral sites. h-TiS_2 may be regarded as a layer structure of these interconnected octahedra as illustrated in the top part of Fig. 9.16. In the van der Waals gap between the TiS_2 layers (ABA sequence) Li may easily be intercalated at any concentration x to form a stage-1 compound h-Li_xTiS_2 ($0 < x \leq 1$). The intercalated Li atoms are at rest at octahedral sites [54]. The cubic polymorph c-TiS_2 can be obtained [60,61] from h-TiS_2 by moving one quarter of the Ti atoms to the van der Waals gap as indicated in the lower part of Fig. 9.16. The ABA stacking is then shifted to a stacking of the type ABCA. Li insertion is possible again in the whole concentration range

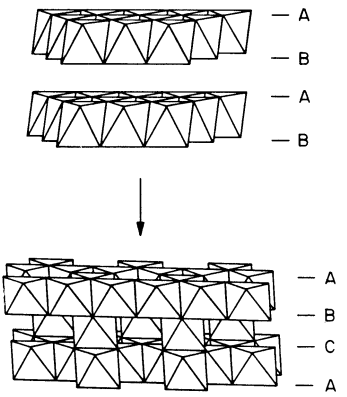

Fig. 9.16. Structure of h-TiS_2 (top), the 2D modification, and of c-TiS_2 (bottom), the cubic modification of the host material. The latter may be derived from h-TiS_2 by shifting the layers from hexagonal closed packed to cubic closed packed anion packing and moving one quarter of the Ti to interlayer octahedra [60].

yielding c-Li_xTiS_2 ($0 < x \leq 1$) and leads to the occupation of the empty octahedra. It is noted that c-TiS_2 irreversibly transforms to h-TiS_2 above 700 K.

SLR was investigated by ^{7}Li-NMR on polycrystalline samples of both modifications at Li concentrations between $x = 0.35$ and $x = 1$ [62]. By use of a Bruker MSL100 spectrometer and a tunable (0 – 7 T) cryomagnet spin-lattice relaxation times both in the laboratory frame (T_1) and in the rotating frame ($T_{1\rho}$) were measured at various fields B_0 and B_1, respectively, (cf. Sect. 9.3). The temperatures of the hexagonal and the cubic samples were varied up to 950 K and 700 K, respectively.

Figs. 9.17 and 9.18 show examples of the T dependence of T_1^{-1} at two frequencies for different Li concentrations. In both modifications diffusion-induced T_1^{-1} peaks are observed.

On the high-T side, T_1^{-1} does not depend on frequency in the case of the cubic modification, which verifies that diffusion is 3D (cf. Sect. 9.2). For the hexagonal polymorph a distinct frequency dependence is found which indicates low-D diffusion. Figure 9.19 explicitly shows data for T_1^{-1} as a function of B_0 at constant T on the high-T side following the logarithmic frequency dependence expected for 2D diffusion. The characteristics showing up in the frequency and temperature dependence of T_1^{-1} are clearly reflected also by the $T_{1\rho}^{-1}$ result, i. e. at lower frequencies and correspondingly lower temperatures. As an example, Fig. 9.20 shows the B_1 dependence of $T_{1\rho}^{-1}$ at a temperature on the high-T side of the $T_{1\rho}^{-1}$ peak. Again a logarithmic frequency dependence is verified over nearly two orders of magnitude. Taken together, the T_1^{-1} and $T_{1\rho}^{-1}$ results on the frequency dependence at high T confirm the logarithmic law in different frequency regimes, which span a total range of five orders of magnitude, and unambiguously show that diffusion is 2D in h-Li_xTiS_2 and 3D in c-Li_xTiS_2.

On the low-T side, T_1^{-1} shows a frequency dependence for both modifications which can be described by a power law according to (9.5), with the

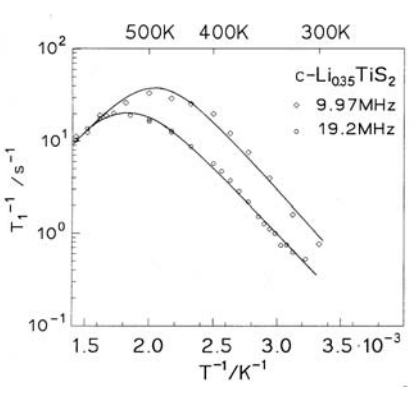

Fig. 9.17. T dependence of the diffusion-induced SLR rate T_1^{-1} in the laboratory frame of ^{7}Li in c-$Li_{0.35}TiS_2$ for two frequencies $\omega_L/2\pi$. The lines are to guide the eye [62].

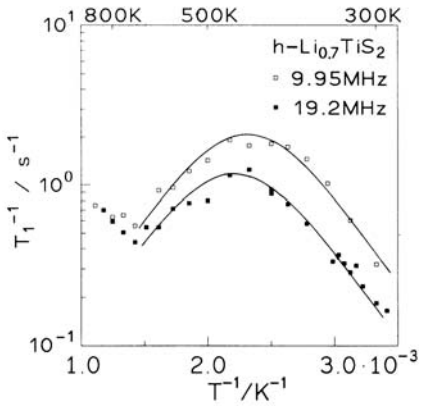

Fig. 9.18. T dependence of the diffusion-induced SLR rate T_1^{-1} in the laboratory frame of ^{7}Li in h-$Li_{0.7}TiS_2$ at two frequencies $\omega_L/2\pi$. The lines are to guide the eye and represent symmetrical curves with respect to the rate maximum [62].

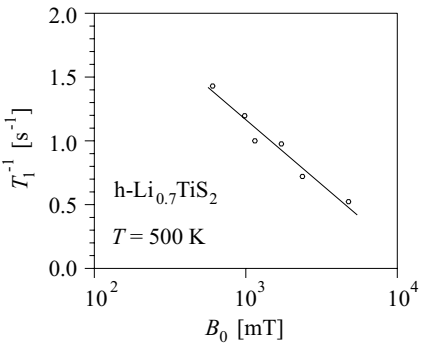

Fig. 9.19. B_0 dependence of the SLR rate in the laboratory frame of ^{7}Li in h-$Li_{0.7}TiS_2$ on the high-T side of the diffusion-induced peak. The solid line represents a logarithmic frequency dependence according to a 2D diffusional process.

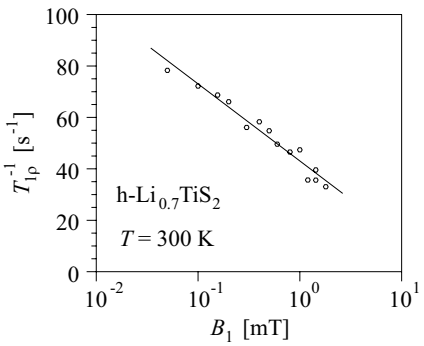

Fig. 9.20. B_1 dependence of the SLR rate in the rotating frame of ^{7}Li in h-$Li_{0.7}TiS_2$ on the high-T side of the diffusion-induced peak. The solid line represents a logarithmic frequency dependence according to a 2D diffusional process [62].

exponent $\alpha \approx 1.3$ both for h-$Li_{0.7}TiS_2$ and c-$Li_{0.6}TiS_2$. This value is significantly smaller than $\alpha = 2$, expected regardless of dimensionality. Similar to the case of the Li graphite intercalation compounds this is in accordance with various theoretical approaches [28–30] where the weak frequency dependence is ascribed to highly correlated diffusion. According to (9.7) and the

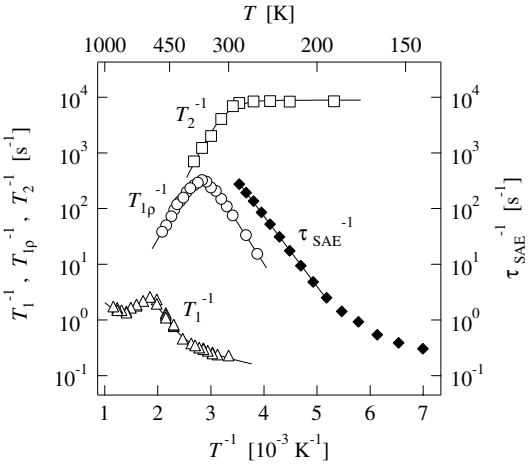

Fig. 9.21. Temperature dependence of the relaxation rates T_1^{-1}, $T_{1\rho}^{-1}$, T_2^{-1} (left-hand ordinate) and of the correlation rate τ_{SAE}^{-1} (right-hand ordinate) obtained from spin-alignment echo (SAE) measurements, for ^{7}Li in h-$Li_{1.0}TiS_2$. T_1^{-1} and $T_{1\rho}^{-1}$ were measured at 10 MHz and 20 kHz, respectively. For the spin-lattice relaxation rate T_1^{-1} a background is visible on which the diffusion-induced peak is superimposed (after [66]).

schematic representation in Fig. 9.3 an exponent $\alpha < 2$ also leads to a smaller (absolute) slope of $\log T_1^{-1}$ vs. $1/T$ on the low-T side. On the other hand, for 2D diffusion the slope of the high-T side will be reduced as compared to the BPP case (cf. Fig. 9.3). If the effects of correlated and 2D diffusion come together, experimentally a pseudo-symmetric peak may be found which, indeed, is the case for h-$Li_{0.7}TiS_2$ (Fig. 9.18, for the corresponding $T_{1\rho}^{-1}$ data see Fig. 3 in [62]). Apparent activation energies $E_{\mathrm{NMR}}^{\mathrm{lT}}$ obtained from the slope of the low-T side are around 0.3 eV for the various samples. This agrees with an early result for h-Li_xTiS_2 obtained by $T_{1\rho}^{-1}$ measurements [63]. From the condition for $T_1^{-1}(T)$ and $T_{1\rho}^{-1}(T)$ maxima ($\omega_{\mathrm{L}}\tau_{\mathrm{c}} \approx 1$ and $\omega_1\tau_{\mathrm{c}} \approx 0.5$, respectively; see Sect. 9.2) and the temperature values where they occur for the various measuring frequencies the important conclusion was drawn that at comparable Li content in the two modifications the jump rate in the interfacial planes of h-Li_xTiS_2 is higher than in the 3D pathways of the cubic polymorph [62].

The large range of frequencies and correlation (or jump) rates probed by T_1^{-1} and $T_{1\rho}^{-1}$ studies[1] can be further extended by T_2^{-1} measurements. An example is shown in a joint representation for h-$Li_{1.0}TiS_2$ in Fig. 9.21 [66].

[1] The gap between the frequency and correlation rate regimes covered by T_1^{-1} and $T_{1\rho}^{-1}$ studies is bridged in certain cases by β-NMR T_1^{-1} measurements [17] as well as by field cycling NMR relaxometry [38].

Though it reflects the main features shown in Fig. 9.5 it has to be kept in mind that in the case of 2D diffusion present here there are deviations from the 3D case. Additionally the figure shows on the right-hand ordinate correlation rates determined by the spin-alignment echo (SAE) technique which is sensitive to ultraslow motions with correlation rates of the order of $1\,s^{-1}$ [64–66]. These correlation rates can be attributed to local jumps between inequivalent sites being characterized by different electric field gradients. These may be identified with two sites in the van der Waals gap, namely the octahedral one, normally occupied by Li, and the tetrahedral one [66]. According to quantum chemical calculations the field gradient at the tetrahedral site differs from that at the octahedral site by a factor of three [67]. Altogether, correlation rates have been covered over nine decades which, as far as NMR studies of Li ion conductors are concerned, seems to have been exceeded up to now only in a β-NMR investigation of Li_3N [11, 68].

Concluding this section, we recall the importance of frequency variation in NMR relaxation measurements to disentangle effects of dimensionality and correlation.

9.6 Nanocrystalline Materials

Another class of interface-dominated systems is represented by nanocrystalline materials [4, 5, 9]. They have been the topic of broad research activity aiming both at a better understanding of the fundamental aspects and at new applications. In contrast to intercalation compounds where an ordered stacking sequence of host and guest layers prevails, nanocrystalline materials consist of an assembly of randomly oriented nanometer-sized crystal grains and of interfacial regions. From an atomistic point of view two types of sites occur, those in the nearly perfect crystallites and those in the highly defective grain boundary regions characterized by a distribution of interatomic distances. This is illustrated in a very simplified way in the left part of Fig. 9.22 where the full and open circles denote chemically identical atomic species. An alternative approach is to regard nanocrystalline materials as consisting of a crystalline phase and an interfacial phase with pores as depicted in the middle part of Fig. 9.22. There is presently no generally accepted model representing all aspects of nanocrystalline materials. A high-resolution transmission electron micrograph of nanocrystalline CaF_2 with an average crystallite size of 9 nm [9, 69] is shown in the right part of Fig. 9.22.

From the broad range of preparation techniques [4] here only two will be regarded. Nanocrystalline materials can be built up from their atomic or molecular constituents or, starting from the other extreme, they are obtained by milling the polycrystalline educt. An example of the former is the inert gas condensation technique. The material is evaporated in an inert gas atmosphere where it thermalizes and precipitates on a cold finger. Then it is gathered and compacted under high pressure (up to 5 GPa). An example of

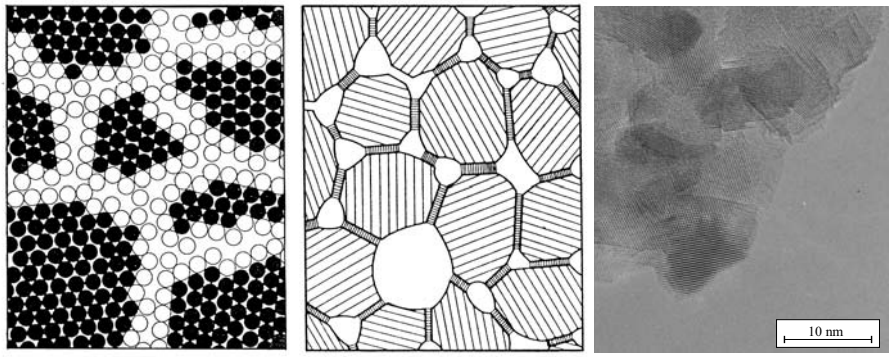

Fig. 9.22. Schematic representations and transmission electron micrograph of nanocrystalline materials. Left: Atoms in crystalline regions (full circles) and in grain boundary regions (open circles) [4]. Middle: Nanocrystalline material consisting of a crystalline phase, the interfacial phase and pores [70]. Right: High-resolution transmission electron micrograph of nanocrystalline CaF_2 with an average grain size of about 9 nm [9].

the alternative route is high-energy ball milling, where the grain size of the microcrystalline starting material is reduced by mechanical attrition [71–73]. The size of the grains is controlled by the duration of the milling process. The excess energy is stored in the grain boundary regions by a highly disordered atomic arrangement.

Here investigations on nanocrystalline CaF_2 (n-CaF_2), prepared by the inert gas condensation technique, and on nanocrystalline $LiNbO_3$, $Li_{0.7}TiS_2$ and $(1-x)Li_2O{:}xB_2O_3$ composites, prepared by high-energy ball milling, will be discussed.

9.6.1 Nanocrystalline Calcium Fluoride

The average grain diameter of the n-CaF_2 material obtained with the inert gas condensation technique was about 9 nm according to X-ray diffraction line broadening and transmission electron microscopy (TEM), see right part of Fig. 9.22. After compaction the density was 96 % of that of single crystalline CaF_2.

Single- or polycrystalline CaF_2 is a F^--ion conductor and the dominant self-diffusion mechanism at elevated temperatures consists of F^--jumps via thermally activated vacancies in the anion sublattice. Fig. 9.23 shows the diffusion-induced peak of T_1^{-1} of ^{19}F in a CaF_2 single crystal (s-CaF_2) [74] including a temperature-independent background, which becomes apparent at low temperatures, in comparison with the SLR rate in n-CaF_2 [75]. For the latter several temperature runs were made, which will be discussed below.

Though measured at a higher Larmor frequency, the SLR rate in n-CaF_2 rises to a peak at considerably lower temperatures than in s-CaF_2. The ac-

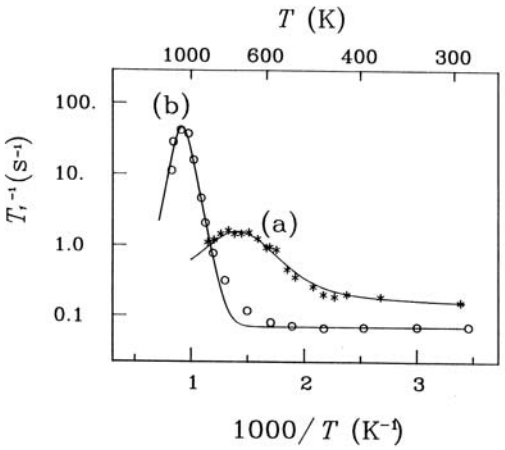

Fig. 9.23. Temperature dependence of the spin-lattice relaxation rate T_1^{-1} of ^{19}F in (a) nanocrystalline CaF_2 ($\omega_L/2\pi = 47\,MHz$, second temperature run) [75] and (b) single-crystalline CaF_2 ($\omega_L/2\pi = 15\,MHz$, data points from [74]). The solid lines are fits of a simple spectral density function as guide to the eye.

tivation energy estimated from the slope of the peak is found to be reduced to typically 0.4 eV compared to 1.6 eV in s-CaF_2. These findings indicate a drastically enhanced F^--diffusivity which is ascribed to the influence of the interfacial regions. A realistic estimate of the enhancement at, e. g., 500 K where the diffusion coefficient in s-CaF_2 itself is increased due to the presence of extrinsic vacancies in addition to the thermal ones (cf. the deviation of the SLR data from the fit curve (b) in Fig. 9.23) can be obtained from a comparison of the corresponding conductivities of n-CaF_2 and s-CaF_2 [76]. The ratio amounts to about 10^4.

Up to temperatures $T \leq 500\,K$, measured values of the SLR rate in n-CaF_2 are reproducible in different $T_1^{-1}(T)$ runs. For higher T, the SLR rate reduces upon thermal cycling and approaches that of s-CaF_2 due to substantial grain growth. A similar observation of thermal metastability and instability, respectively, was made in $T_{1\rho}$ measurements on ^{63}Cu in n-Cu [77]. The activation energies observed in n-CaF_2 in successive temperature runs increase towards the value for s-CaF_2. TEM of the n-CaF_2 material after three $T_1^{-1}(T)$ runs up to 870 K showed growth of the average grain diameter to about 50 nm [69].

Further information on the fast interfacial diffusion was obtained from temperature-dependent lineshape measurements as shown in Fig. 9.24 [75]. At room temperature the ^{19}F resonance can be described by a broad Gaussian line (Fig. 9.24a[2]). This corresponds to the rigid lattice. As the temperature

[2] The small dip in the line centre is due to a dead time effect at the start of the FID recording.

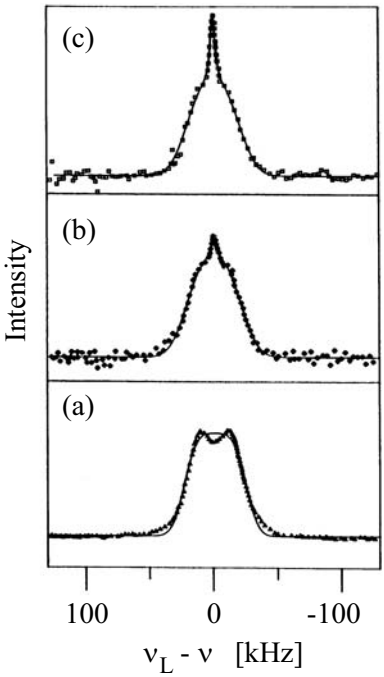

Fig. 9.24. NMR lineshapes of ^{19}F in an as-prepared nanocrystalline CaF_2 sample at 298 K (a), 400 K (b), and 440 K (c) at $\omega_L/2\pi = 24$ MHz. The lines through the data represent fits by a Lorentzian and/or a Gaussian.

of the virgin sample is raised up to 440 K the width of the broad line remains essentially constant and a superimposed motionally narrowed line shows up

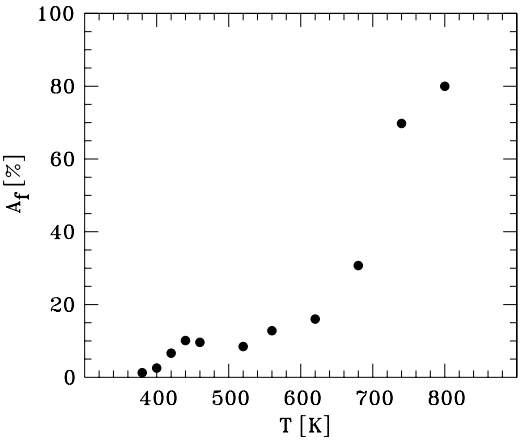

Fig. 9.25. Fraction A_f of the motionally narrowed ^{19}F signal with respect to the total signal intensity in n-CaF_2 as a function of temperature. Between about 440 K and 600 K a T independent fraction of mobile ions corresponding to the mass fraction of the interfacial regions is observed.

which can be described by a Lorentzian (Fig. 9.24b,c). The two components whose centres of gravity coincide are attributed to the stationary fluorine ions in the grains and the highly mobile ones in the interfacial regions.

Fig. 9.25 shows the fraction A_f of the area under the Lorentzian line with respect to the total lineshape area. A_f corresponds to the fraction of mobile F^-. At 440 K the narrowed line has attained about 10 % of the signal intensity and remains constant up to about 600 K where the onset of line narrowing also in the grains is observed. The plateau value of A_f should reflect the mass fraction of the interfacial regions. Taking their reduced mass density into account (cf. Sect. 9.1) the volume fraction is somewhat higher than 10 % but still smaller than the value of 25 % which may be estimated [5] using the XRD result for the average grain diameter. The difference may be attributed to different weighting of interfacial and crystal regions in the dynamic and static measurements, respectively.

First measurements on the analogous system n-BaF_2 [78], which, however, was not prepared by inert-gas condensation but by high-energy ball milling, show SLR results which are consistent with those on n-CaF_2 presented above.

9.6.2 Nanocrystalline, Microcrystalline and Amorphous Lithium Niobate

In spite of the extensive research work performed on $LiNbO_3$ mainly because of its technical relevance, e. g. in electro-optic applications, NMR investigations of the Li ion dynamics have been rather scarce. Thus for comparison reasons not only nanocrystalline $LiNbO_3$, prepared by high-energy ball milling, but also the coarse-grained polycrystalline source material (i.e. microcrystalline $LiNbO_3$, m-$LiNbO_3$) and amorphous $LiNbO_3$ (a-$LiNbO_3$) were studied in detail [79–81]. Fig. 9.26 shows results of ^{7}Li $T_1^{-1}(T)$ measurements at various frequencies in the MHz regime on n-$LiNbO_3$ with an average grain diameter of 23 nm and on m-$LiNbO_3$ (average grain size of some μm) at one of the above frequencies for comparison. For both modifications only the low-T sides of the diffusion-induced $T_1^{-1}(T)$ peaks, being superimposed on background relaxation rates, were observable in the accessible temperature ranges up to 1400 K and 500 K, respectively. From the shift of the flank to lower T it can be concluded that in n-$LiNbO_3$ the effective correlation time τ_c is by orders of magnitude smaller, i. e. diffusion is much faster. The slopes indicate that the activation energy is reduced from 0.75 eV for m-$LiNbO_3$ to about one third of this value.

Figure 9.27 shows an Arrhenius plot of the SLR rate in the rotating reference frame at various frequencies in the kHz regime for m-$LiNbO_3$. Instead of conventional $T_{1\rho}^{-1}$ (cf. Sect. 9.3) the SLR rate T_{1e}^{-1} in the pulsed rotating frame, being a time saving alternative [82], was measured. In this case also the maxima of the curves and parts of their high-temperature sides were detectable. From the T_{1e}^{-1} maximum for a given frequency an absolute value for τ_c in m-$LiNbO_3$ can be estimated which amounts at, e. g., 890 K to

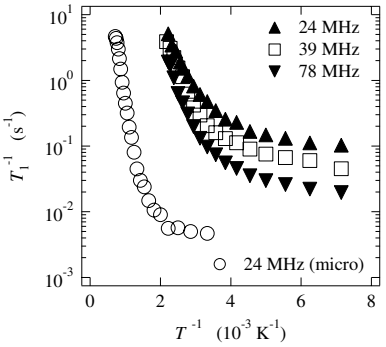

Fig. 9.26. ^{7}Li SLR rate versus inverse temperature in n-$LiNbO_3$ at three frequencies measured in the laboratory reference frame. For comparison the T_1^{-1} results from m-$LiNbO_3$ at $\omega_L/2\pi = 24\,\mathrm{MHz}$ are displayed, too [79, 80].

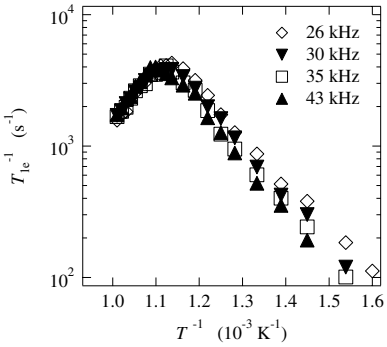

Fig. 9.27. ^{7}Li SLR rate versus inverse temperature in m-$LiNbO_3$ at four frequencies measured in the pulsed rotating frame [79, 80].

$3 \cdot 10^{-6}\,\mathrm{s}$. For uncorrelated jumps this corresponds to a diffusion coefficient $D = 8 \cdot 10^{-15}\ \mathrm{m^2\,s^{-1}}$ as obtained from the Einstein-Smoluchowski equation (see (1.36) in Chap. 1). For the mean square displacement the Li-Li distance of about 0.38 nm in the crystal structure of $LiNbO_3$ was adopted and the dimensionality of the jump process is taken to be three because the SLR rate on the high-T side is independent of frequency (Fig. 9.27, cf. Table 9.1). The activation energy of 0.88 eV obtained from the high-T side, which applies to long-range diffusion, is greater than the value 0.75 eV from the low-T side which agrees with that from the T_1^{-1} measurements and reflects short-range motion. The asymmetry of the $T_{1e}^{-1}(T)$ peak corresponds qualitatively to a frequency dependence on the low-T side described by $\alpha < 2$; this is also found for the SLR rate in the laboratory frame both for microcrystalline and nanocrystalline $LiNbO_3$. Quantitatively, however, (9.7) is not fulfilled.

In additon to the SLR measurements also lineshape measurements were done [80, 81, 83]. Fig. 9.28 shows the lineshape obtained in n-$LiNbO_3$ in comparison with m-$LiNbO_3$ and a-$LiNbO_3$. We focus on the central line of the spectrum of ^{7}Li ($I = 3/2$). The figure shows the motional narrowing for all three samples. Similar to the ^{19}F spectrum in n-CaF_2 (Fig. 9.24), the central line of ^{7}Li in n-$LiNbO_3$ reveals a superposition of two distinct contributions already at moderate temperatures (Fig. 9.28, middle row). The narrow component is caused by Li ions mobile at 450 K in the interfacial regions whereas the broad line can be attributed to Li ions within the grains being still immobile at that temperature. In contrast, the spectra of m-$LiNbO_3$ (Fig. 9.28, bottom row) do not show a comparable structuring at any temperature indi-

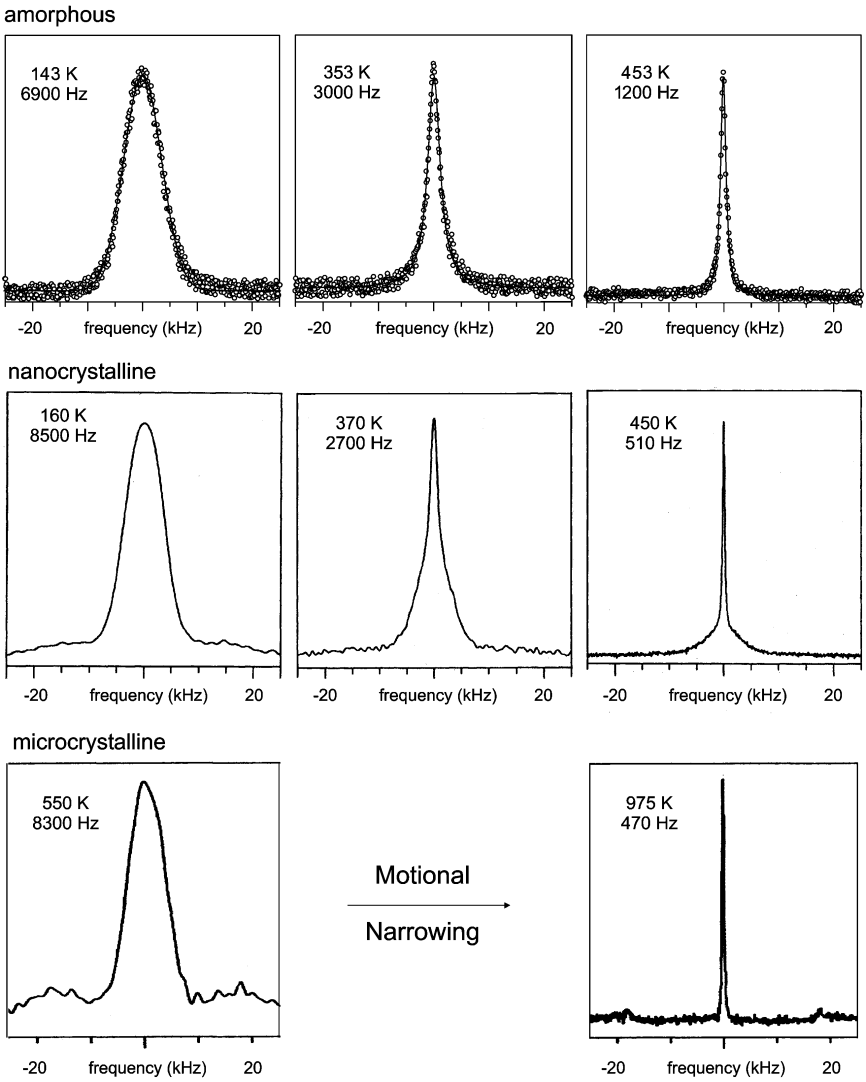

Fig. 9.28. Shape of the central line of the ^{7}Li-NMR spectrum. Top row: signal of a-$LiNbO_3$ at 143 K, 353 K and 453 K. Middle row: signal of n-$LiNbO_3$ at 160 K, 370 K and 450 K. Bottom row: signal of m-$LiNbO_3$ at 550 K and 975 K. The frequencies denote the linewidths (FWHM) [81].

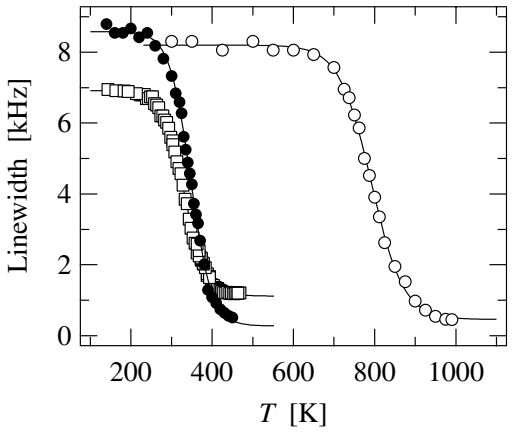

Fig. 9.29. Temperature dependence of the ^{7}Li linewidth in n-$LiNbO_3$ (full circles), m-$LiNbO_3$ (open circles) and amorphous $LiNbO_3$ (squares). The lines show fits yielding activation energies [81].

cating equivalent sites, i. e. a line contribution from bulk material only. For comparison Fig. 9.28 (top row) also shows the motional narrowing in the amorphous material. It starts at temperatures similar to those in n-$LiNbO_3$, but the lineshape has no comparable structure. This indicates that, as expected, the amorphous material is homogeneously disordered in contrast to n-$LiNbO_3$ where heterogeneous disorder is found. Fig. 9.29 displays the effective linewidth of the n- , m- and a-material as a function of temperature. Motional narrowing for Li ions in the interfacial regions of the nanocrystalline material starts at a temperature some 400 K below that in the undisturbed crystal and very similar to that in the amorphous material. The T dependence of the linewidth, analyzed with a phenomenological equation [84], yields an activation energy of 0.39 eV for n-$LiNbO_3$, 1.25 eV for p-$LiNbO_3$ and 0.35 eV for a-$LiNbO_3$. These values are in reasonable agreement with those obtained by SLR measurements on the same samples and suggest that the fast diffusion pathways in the interfacial regions of nanocrystalline $LiNbO_3$ being prepared by ball milling are similar to those in the amorphous material.

A further source of information not discussed here are the quadrupole satellites in the ^{7}Li spectra.

9.6.3 Nanocrystalline Lithium Titanium Disulfide

In Sect. 9.5.2 ^{7}Li spin-lattice relaxation results on microcrystalline hexagonal $Li_{0.7}TiS_2$ were presented in comparison with those on the corresponding cubic modification. We now turn to a study of nanocrystalline hexagonal $Li_{0.7}TiS_2$ and compare it with the above microcrystalline reference material from which it was produced by ball milling. Furthermore nanocrystalline

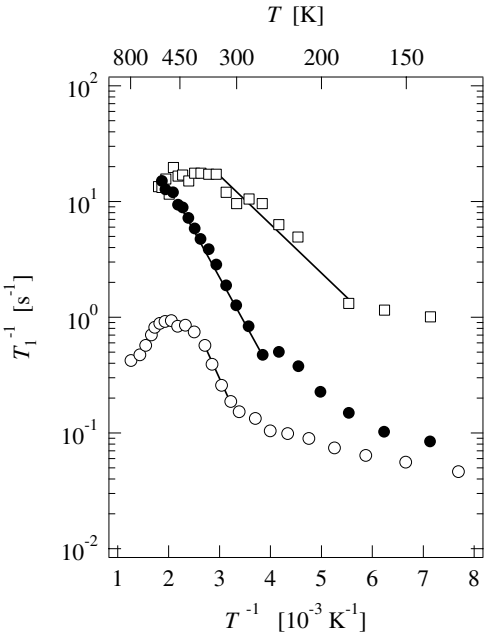

Fig. 9.30. Relaxation rates T_1^{-1} of microcrystalline (open circles), nanocrystalline (full circles) and amorphous (squares) Li_xTiS_2 at $\omega_L/2\pi = 24.5\,MHz$ [85].

$Li_{0.7}TiS_2$ is compared with amorphous $Li_{0.7}TiS_2$ [85]. An Arrhenius plot of T_1^{-1} for all three forms is shown in Fig. 9.30. Contrary to the case of $LiNbO_3$ (Sect. 9.6.2), the activation energy in nanocrystalline $Li_{0.7}TiS_2$, estimated from the slope of the low-temperature flank to be about 0.2 eV, is not considerably smaller than that in the microcrystalline material and larger than that in the amorphous one (about 0.1 eV). This indicates that the diffusion pathways in the two crystalline forms are similar and determined by the layer structure of the grains, even if the interfacial regions are essentially amorphous, while in the bulk amorphous phase the less dense packing may be responsible for the reduction of the activation energy. The spin-lattice relaxation rate measured after annealing a freshly prepared nanocrystalline Li_xTiS_2 sample at various temperatures was also used to study the kinetics of the Li intercalation process [85].

Concerning the frequency dependence of T_1^{-1} in the regime of the low-temperature flank of the diffusion-induced peaks for the nanocrystalline and the amorphous forms, the exponent α (cf. (9.5)) was found to be smaller than 1 (approximately 0.6). This result for the two disordered forms contrasts with that for microcrystalline h-$Li_{0.7}TiS_2$ where α was larger than one (approximately 1.3, see Sect. 9.5.2). Sublinear frequency dependencies have also been observed in ionic glasses by NMR (e. g. [86–88]) as well as β-NMR [56, 89, 90] (cf. Sect. 9.7). In [86] $\alpha < 1$ was interpreted in the frame

of the coupling concept [28] as being due to spin-lattice relaxation by localized ion motion involving two-level systems, typical of disordered systems. A sublinear frequency dependence of the motion-induced relaxation rate corresponds to a superlinear frequency dependence of the ionic conductivity (see Chap. 20) which has also been observed in disordered systems (e. g. [92]). Such a behaviour has also been treated in terms of the concept of mismatch and relaxation treated in Chap. 21 (cf. [29]).

9.6.4 Nanocrystalline Composites of Lithium Oxide and Boron Oxide

Besides single-phase nanocrystalline materials also composite systems of an ionic conductor and an insulator have been studied. Such systems are called dispersed ionic conductors and can show surprising effects in the overall conductivity [93–96] (see also Sect. 22.9.2 of Chap. 22). Fig. 9.31 shows a sketch of such a composite material consisting of two different types of grains which are shown as light grey and dark grey hatched areas for the ionic conductor and the insulator, respectively. There are now three different types of interfaces. These are interfaces between ionic conductor grains (dotted lines), interfaces between insulator grains (dashed lines) and interfaces between an ionic conductor and an insulator grain (solid lines). The latter ones seem to play a crucial role for the overall conductivity in many dispersed ionic conductors [97–102]. The composition and the grain sizes of such composites can easily be varied which gives the possibility to modify the network of the different interfaces which in turn might lead to materials with tailored macroscopic properties.

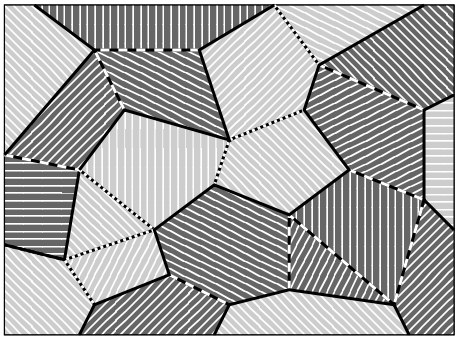

Fig. 9.31. Sketch of a composite material of ionic conductor grains (light grey areas) and insulator grains (dark grey areas). The network of interfaces consists of interfaces between ionic conductor grains (dotted lines), interfaces between insulator grains (dashed lines) and interfaces between ionic conductor and insulator grains (solid lines).

In order to study the dynamics of Li ions in such composites, among others ^{7}Li NMR lineshape measurements on nanocrystalline $(1-x)Li_2O{:}xB_2O_3$ at, e. g., $x = 0.5$ and a temperature of 433 K were performed [103]. The central line shows two contributions similar to the results found for nanocrystalline CaF_2 (Sect. 9.6.1) and nanocrystalline $LiNbO_3$ (Sect. 9.6.2) which again can be attributed to fast and slow Li ions in the interfaces and the bulk of the grains, respectively. The microcrystalline counterparts again show only one broad line.

This is consistent with the time dependence of the free induction decay (FID) found for this composite material at 433 K (Fig. 9.32). The microcrystalline material (Fig. 9.32(a)) shows only one fast decaying part in the time regime below 50 μs which can be described by $\exp(-a_1 t^2)\sin(a_2 t)/a_2 t$ (cf. [13]), with a_1 and a_2 being fit parameters. For the nanocrystalline material (Fig. 9.32(b)) this component is also present, but now there is an additional slowly decaying component (marked by an arrow), which becomes apparent for times larger than 100 μs and can be described by a simple exponential function. Of course, the NMR lineshapes are the Fourier transforms of these FIDs and one can easily show that the fast decaying component in the FID belongs to a broad component in the NMR lineshape and the slowly decaying component in the FID belongs to a motionally narrowed component. These are attributed to the slow ions in the grains and the fast ones in the interfacial regions, respectively. For the microcrystalline sample only Li ions in the grains can be detected because the number fraction of Li ions in the interfacial regions is too small. The fact that for the nanocrystalline composite material the two different Li species can be discriminated by their different time dependences in the FID is due to their different T_2 values.

Another way to discriminate the two Li species is via their different T_1 values. Fig. 9.33 shows the magnetization transients of the micro- and the nanocrystalline composites. Whereas for the microcrystalline material the magnetization transients $M(t)$ can be described by a monoexponential function, the nanocrystalline composite shows significant deviation from monoexponential behaviour and has to be described by a sum of two exponential functions reflecting the fact that the fast and slow Li species have different T_1 values. This also reveals that in the present case spin diffusion between the two Li reservoirs is not fast enough for a homogeneous averaging to set in which would result in a monoexponential magnetization behaviour (cf. Sect. 9.7.1). Spin diffusion becomes apparent only in the fact that the relaxation time of the slow Li ions in the nanocrystalline composite is slightly reduced in comparison with the corresponding microcrystalline composite (see values given in Fig. 9.33).

Fig. 9.34 shows the temperature dependence of the spin-lattice relaxation rates of the fast and the slow Li ions of nanocrystalline $(1-x)Li_2O{:}xB_2O_3$, $x = 0.5$. The slope of the Arrhenius fits which represent the low-temperature flanks of the corresponding diffusion-induced peaks yield the activation bar-

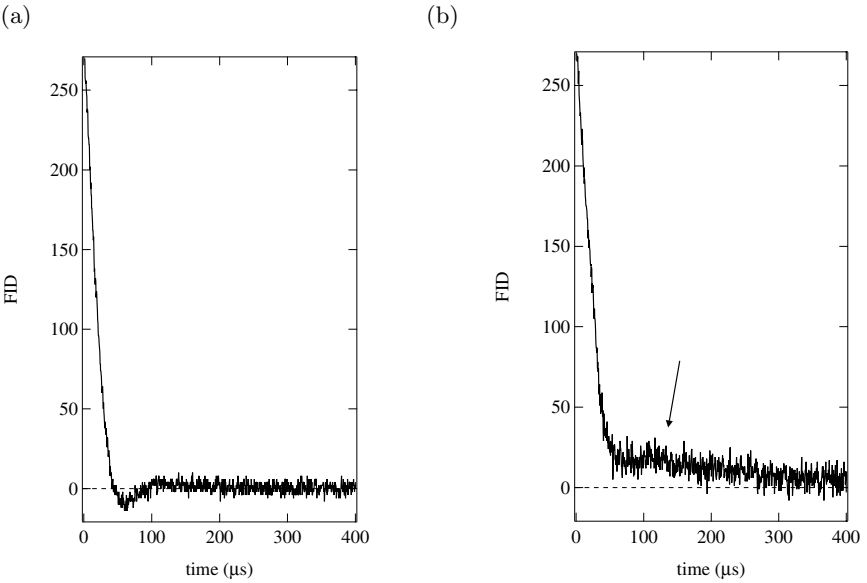

Fig. 9.32. Free induction decay of ^{7}Li in (a) microcrystalline and (b) nanocrystalline $(1-x)Li_2O{:}xB_2O_3$, $x = 0.5$, at 58 MHz and 433 K. The arrow indicates a slowly decaying component in the case of the nanocrystalline material which is not present for the microcrystalline sample.

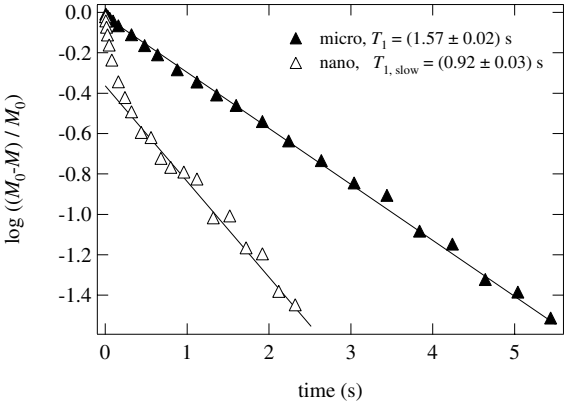

Fig. 9.33. Magnetization transients of ^{7}Li in microcrystalline and nanocrystalline $(1-x)Li_2O{:}xB_2O_3$, $x = 0.5$, at 58 MHz and 433 K. The lines represent a monoexponential fit in the case of the microcrystalline material and the slow component of a biexponential fit in the case of the nanocrystalline material.

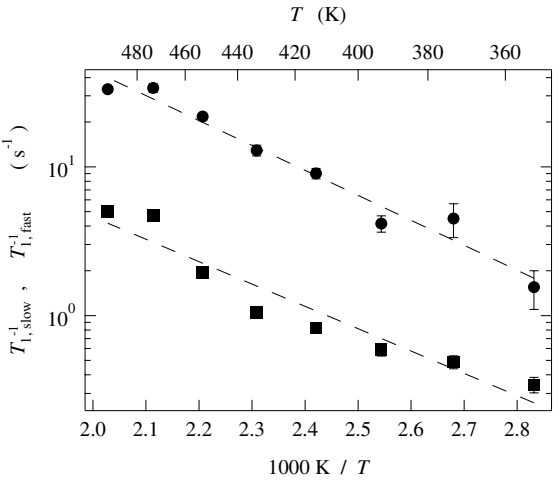

Fig. 9.34. Discriminated fast and slow relaxation rates T_1^{-1} of ^{7}Li in nanocrystalline $(1-x)Li_2O{:}xB_2O_3$, $x = 0.5$, at 58 MHz. The dashed lines represent Arrhenius fits.

riers for single ion jumps. Within the experimental errors they are the same for the slow and the fast Li ions. Therefore the different diffusivities of the two species of Li ions are not caused by an enhanced mobility but by an enhanced concentration of defects in the neighbourhood of the interfaces.

In summary, the different diffusivities of the two Li species in the nanocrystalline composites become apparent in three different results: (i) two contributions to the NMR lineshape, (ii) two contributions to the FID and (iii) two components in the magnetization transients. In all cases the microcrystalline composites show only one species of Li ions.

The effects described in this section for the composites of Li_2O and B_2O_3 can be also found in pure nanocrystalline Li_2O but they are much weaker there. This shows that an interface between unlike crystallites generates a larger number of Li ions than an interface between Li_2O grains.

It is remarkable that results for the analogous system $(1-x)Li_2O{:}xAl_2O_3$ are very similar to those presented in this section [104]. This suggests that it is not important which specific insulator is added to Li_2O and that the results reveal a generic behaviour of such composites.

9.7 Glasses

In the previous section on nanocrystalline materials, systems with heterogeneous disorder were studied. We now turn to materials with homogeneous disorder. First the question how local disorder influences the decay behaviour of the nuclear polarization of the probe nuclei in β-NMR relaxation is

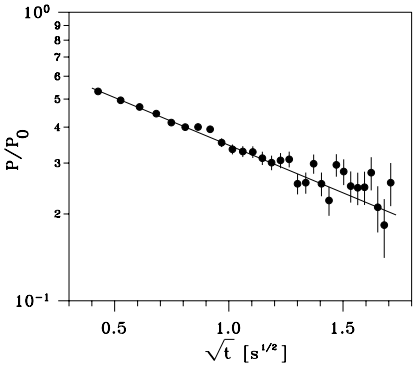

Fig. 9.35. Time dependence of the polarization of ^{8}Li in $Li_2O \cdot 3\,B_2O_3$ glass at $T = 120\,K$, $B_0 = 37\,mT$. The solid line represents a fit with $P/P_0 = \exp(-\sqrt{t/T_{1inh}})$.

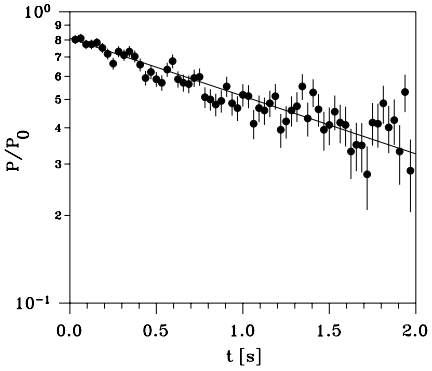

Fig. 9.36. Time dependence of the ^{8}Li polarization in the glassy electrolyte solution $LiCl \cdot 4\,D_2O$ at $T = 10\,K$, $B_0 = 300\,mT$. The solid line represents a fit with $P/P_0 = \exp(-t/T_{1hom})$.

addressed. The answer will be exemplified by experimental results on glasses with different short-range order. In the next subsection direct comparison of homogeneously disordered systems with their ordered counterparts will be made using, as example, lithium aluminosilicates where compounds with identical compositions in the glassy and the crystalline state can easily be prepared. The comparison will be based on ^{7}Li-NMR and ^{8}Li-β-NMR relaxation studies.

9.7.1 Inhomogeneous Spin-Lattice Relaxation in Glasses with Different Short-Range Order

In the study of SLR in materials with structural disorder – whether homogeneous or heterogeneous – the question arises if the relaxation behaviour of nuclei on inequivalent sites can be discriminated. This was possible, e. g., in the case of the ^{7}Li-NMR T_1 measurements on nanocrystalline Li_2O:B_2O_3 composites reported in Sect. 9.6.4 where spin diffusion did not play an important role. Often, however, in conventional NMR measurements on homogeneous systems polarization transfer among neighbouring nuclei by resonant mutual spin flips, i. e. spin diffusion, will hamper such a discrimination. In β-NMR the highly diluted probe nuclei differ in their magnetogyric ratio γ from the surrounding stable nuclei and thus relax independently without resonant polarization transfer (cf. Sect. 9.4).

Two classes of glassy systems were investigated with the β-NMR method. These are on the one hand oxide glasses represented here by the borate glass $Li_2O \cdot 3\,B_2O_3$ and on the other hand electrolyte glasses exemplified by the solution $LiCl \cdot n\,D_2O$ ($n = 4$ and 7).

As shown in Fig. 9.35 the polarization $P(t)$ of ^{8}Li in the borate glass decays non-exponentially and can well be represented by

$$P(t) = P_0 \cdot \exp\left[-\sqrt{t/T_{1\mathrm{inh}}}\right] \quad , \tag{9.22}$$

where $T_{1\mathrm{inh}}$ is the so-called inhomogeneous relaxation time to be addressed in the following. Contrary to such a single transient, the bulk of data also allows one to determine the parameter β in the stretched exponential

$$P(t) = P_0 \cdot \exp\left[-(t/T_{1\mathrm{inh}})^{\beta}\right] \quad . \tag{9.23}$$

Taking together, for example, the data on ^{8}Li in $Li_2O \cdot 3\,B_2O_3$ in the temperature range 5 K - 200 K the value $\beta = 0.52(1)$ was found [90]. Furthermore, transients of the polarization of the β-NMR probe ^{12}B in the same glass and again of ^{8}Li in other oxide glasses ($Li_2O \cdot 2\,SiO_2$, $Li_2O \cdot Na_2O \cdot 4\,SiO_2$ and $Li_2O \cdot Al_2O_3 \cdot 4\,SiO_2$) showed a behaviour according to (9.22) [90, 91, 105].

Essential in the explanation of the $\exp(-\sqrt{t/T_{1\mathrm{inh}}})$ law is the fact that an observed transient results from inhomogeneous polarization averaging [106]. The β-NMR probes are isolated and relax independently with different rates

$$1/T_1^{(k)} = \sum_i a(r_{ik})\ J(\omega_\mathrm{L}, \tau_i) \tag{9.24}$$

where $a(r_{ik}) = a_0(r_0/r_{ik})^m$ is the coupling constant of the probe nucleus k to a relaxation centre ('defect') i at distance r_{ik} and $J(\omega, \tau_i)$ is the spectral density function of the field fluctuations attributed to this centre.

Inhomogeneous polarization averaging over all probe nuclei yields

$$P_{\mathrm{inh}}(t) = \left\langle P_0 \exp\left[-t/T_1^{(k)}\right]\right\rangle_k = P_0 \cdot \exp\left[-\left(\frac{t}{T_{1\mathrm{inh}}}\right)^{3/m}\right] \quad . \tag{9.25}$$

For $m = 6$ which applies to dipolar and quadrupolar coupling, the observed $\exp(-\sqrt{t/T_{1\mathrm{inh}}})$ law is obtained. It is noted that homogeneous averaging, which in general is performed in classical NMR relaxation where rapid polarization transfer due to high probe concentration is possible, results in a single exponential

$$P_{\mathrm{hom}}(t) = P_0 \cdot \exp\left[-t/\langle T_1^{(k)}\rangle_k\right] = P_0 \cdot \exp[-t/T_{1\mathrm{hom}}] \quad . \tag{9.26}$$

Contrary to the oxide glasses, β-NMR relaxation in the electrolyte glass $LiCl{\cdot}nD_2O$ ($n = 4$; 7) was found to be monoexponential as illustrated in Fig. 9.36 [53, 107]. The bulk of $P(t)$ data obtained in the glassy state clearly shows that here β is near unity and not 1/2. $LiCl{\cdot}nD_2O$ has a disordered structure consisting of Cl^- ions and $Li^+(4D_2O)$ complexes as basic units. For $n = 7$ the excess water is interstitially incorporated between $Li^+(4D_2O)Cl^-$

clusters. In each case the Li^+ ions are tetrahedrally surrounded by D_2O molecules. Thus, despite the overall amorphous structure, the near neighbourhood of each Li ion is largely equivalent[3]. This contrasts with the oxide glasses, where Li as network modifier (or B as network constituent) occupies many inequivalent sites. This difference in local structure near the probe is the reason for the different transient behaviour of the polarization found in the two classes of glassy systems.

In conclusion, β-NMR relaxation is inherently sensitive to local order and a deviation from monoexponential polarization decay is a fingerprint of the disorder near the probe.

9.7.2 Glassy and Crystalline Lithium Aluminosilicates

Lithium aluminosilicates are of interest for the design of materials with negligible thermal expansion which is possible due to opposite signs of the expansion coefficients in the crystalline and the glassy state [108]. Another point of interest, relevant here, is the lithium conductivity and diffusivity.

In the system Li_2O - Al_2O_3 - $n SiO_2$, Li motions were studied in glasses with $n = 2$; 4; 8, and in their crystalline counterparts β-$LiAlSiO_4$ (β-eucryptite), β-$LiAlSi_2O_6$ (β-spodumene) and $LiAlSi_4O_{10}$ (petalite composition). The ratio of Li_2O to Al_2O_3 is always one, i. e. the charge of each Li^+ is compensated by AlO_4^-. Non-bridging oxygen atoms which interrupt the silicate network in binary oxide glasses with high alkali content are not present in these ternary glasses and their silicate network is fully polymerised. In the following, the discussion is mainly confined to glassy and polycrystalline samples with the spodumene composition ($n = 4$). In the crystal structure of β-spodumene there are four pairs of closely neighboured Li sites per unit cell. Their distance is 0.13 nm and only one site is occupied at a time. The distance between different pairs of Li sites is about 0.45 nm. This suggests two types of possible Li jumps, long-range jumps between different pairs and a localized motion by hops between the sites of a pair.

In Fig. 9.37, ^{7}Li $T_1^{-1}(T)$ data for the glassy and the crystalline sample at one frequency are compared [87]. For both modifications a pronounced diffusion-induced peak shows up which in the case of the glass occurs at roughly 700 K, i. e. some 250 K below the glass transition temperature, and in the case of the crystal at about 820 K. These peaks are due to the long-range Li jumps. The temperature values of the T_1^{-1} maxima and the slopes of the low-T flanks show that the jump rate of Li^+ is faster and the activation energy is smaller in the glass than in the crystal. Similar behaviour was found in the other Li aluminosilicates [88]. The activation energies $E_{\mathrm{NMR}}^{\mathrm{lT}}$ obtained from the slopes of the low-T side of the T_1^{-1} peak, corrected for a

[3] To some extend this type of glass may also be regarded as heterogeneously disordered.

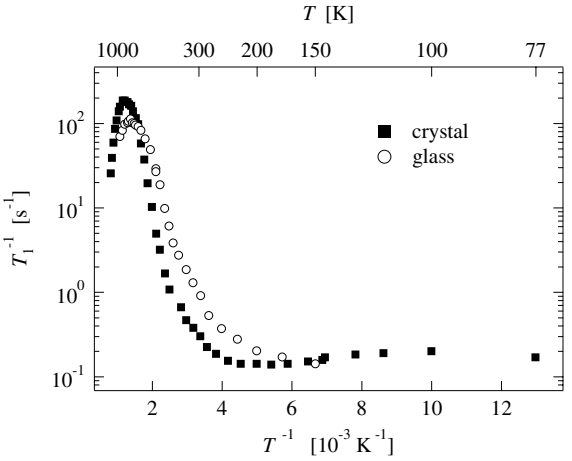

Fig. 9.37. Temperature dependence of T_1^{-1} of ^{7}Li in glassy and polycrystalline $LiAlSi_2O_6$ (β-spodumene) at $\omega_L/2\pi = 38.9$ MHz [87].

small background contribution to T_1^{-1}, are summarized in Table 9.2, neglecting a possible slight frequency dependence. There is no obvious trend with Li concentration. Provided that the diffusion mechanism does not change, a logarithmic decrease of the activation energy with increasing mobile-ion concentration is predicted by various model calculations of diffusion in disordered systems [109–111] (see also Chap. 20).

Inspection of Fig. 9.37 further shows that a peak asymmetry, expected according to Sect. 9.2 for the glass, is also found for the crystal. For crystalline $Li_2O \cdot Al_2O_3 \cdot 4\,SiO_2$ the value $E_{NMR}^{hT} = 0.86(3)$ eV is obtained from the slope of the high-T side [87]. Comparison with the corresponding E_{NMR}^{lT} value in Table 9.2 yields $\alpha = 1.6$ for the parameter in (9.7). For the glass the high-T flank and thus E_{NMR}^{hT} was not accessible. However, as verified for crystalline $Li_2O \cdot Al_2O_3 \cdot 4\,SiO_2$ [112] and generally predicted (e. g. [29]) E_{NMR}^{hT} is essentially equal to the activation energy E_σ^{dc} from dc conductivity measurements

Table 9.2. Activation energies E_{NMR}^{lT} [eV] obtained from the low-T slopes of ^{7}Li SLR rate peaks in glassy and crystalline lithium aluminosilicates with various mineral compositions. The error in E_{NMR}^{lT} is typically 2 in the last digit.

	glass	crystal
$Li_2O \cdot Al_2O_3 \cdot 2\,SiO_2$ (eucryptite)	0.30	0.40
$Li_2O \cdot Al_2O_3 \cdot 4\,SiO_2$ (spodumene)	0.34	0.50
$Li_2O \cdot Al_2O_3 \cdot 8\,SiO_2$ (petalite)	0.22	0.47

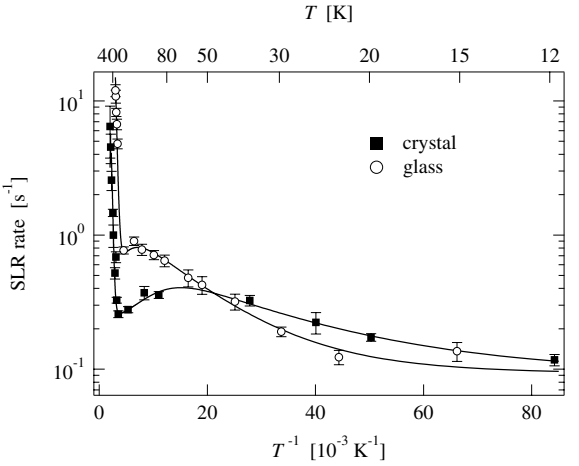

Fig. 9.38. Temperature dependence of the spin-lattice relaxation rate of ^{8}Li in glassy (○) and polycrystalline (■) $LiAlSi_2O_6$ (β-spodumene) at a magnetic field corresponding to $\omega_L/2\pi = 3\,\mathrm{MHz}$. The lines are drawn to guide the eye.

(for a small difference between the two see [113] and Chap. 20). In the case of the glass $E_\sigma^{\mathrm{dc}} = 0.66\,\mathrm{eV}$ was found [112]. Using (9.7), this results in $\alpha = 1.5$. The deviation from standard SLR behaviour [16] is also reflected by a sub-quadratic frequency dependence of T_1^{-1} found on the low-T flank of the peak for both modifications [87]. The experimental power law (cf. (9.5)) is even weaker than that expected on account of the asymmetry of the rate peak (cf. (9.6)) and can be described by $\alpha = 0.9(2)$ and $\alpha = 0.8(1)$ for crystalline and glassy $Li_2O \cdot Al_2O_3 \cdot 4\,SiO_2$, respectively [87]. Thus, in this regard the apparently ordered ion conductor shows nearly the same 'anomalies' as the disordered one. The sublinear frequency dependence being indicated in the glass shows up also in other glasses [86, 88–91] as well as in nanocrystalline ion conductors, e. g. $Li_{0.7}TiS_2$, as mentioned in Sect. 9.6.3.

Besides the main peak at about 820 K, in Fig. 9.37 a second, broad maximum can be seen for the crystalline sample around roughly 100 K. This can be attributed to the short-range hopping of the Li ions between the pair sites mentioned above. Fig. 9.38 shows the corresponding data obtained by β-NMR on ^{8}Li at 3 MHz [114] covering the temperature range from about 500 K down to 10 K. Whereas in the case of polycrystalline $LiAlSi_2O_6$ transients $P(t)$ of the ^{8}Li polarization could be fitted by a single exponential, in the glass $P(t)$ followed the expected $\exp(-\sqrt{t/T_{1\mathrm{inh}}})$ behaviour (9.22). The resulting values of the inhomogeneous relaxation rate $T_{1\mathrm{inh}}^{-1}$ are displayed in Fig. 9.38. For temperatures above 200 K the low-temperature flank of the long-range diffusion induced peak is visible again. The maximum of the relaxation rate due to the localized jumps in crystalline $LiAlSi_2O_6$ occurs at about 70 K. For the glassy material this maximum appears only as a slight

shoulder. Using the temperature of the SLR rate maximum of ^{7}Li together with that of ^{8}Li (Figs. 9.37 and 9.38) one can estimate the activation energy for the jumps between the pair sites in the crystalline material to be roughly 50 meV. This result is also consistent with ^{7}Li-T_1 data obtained at different frequencies [115].

In summary, glassy and crystalline aluminosilicates, besides being interesting for applications, provide a playground for the study of the influence of disorder on ion transport properties by complementary techniques, as exemplified here for the spodumene system.

9.8 Conclusion

In this chapter the use of stable and β-radioactive NMR nuclei for probing diffusive motion was reviewed. After having shown how microscopic information on the diffusive motion can be obtained from the SLR rate, the corresponding NMR and β-NMR techniques were outlined.

The materials discussed in this chapter were Li intercalation compounds as examples of layer-crystalline systems with simple internal interfaces, nanocrystalline ceramics as examples of materials with complex internal interfaces and, finally, oxide glasses representing homogeneously disordered systems. In all three classes the 3D ordered modifications were also examined for comparison.

Emphasis in the SLR investigations was put on the variation of frequency besides temperature. In the case of the intercalation compounds this allowed one to study the high-temperature (low-frequency) limit and to trace in-plane 2D diffusion processes. In all materials of interest here and contrary to the 'ideal' case of Li metal, the frequency dependence of the SLR rate in the low-temperature limit was found to be weaker than that predicted by the standard (BPP) model which was ascribed to the influence of disorder and/or Coulomb interaction. In the nanocrystalline ceramics, in addition to NMR relaxation studies, lineshape measurements helped to elucidate the heterogeneous structure where the interfacial regions provide a network of pathways for fast diffusion. The heterogeneous structure results in heterogeneous dynamics of the mobile ions with fast ions in the interfacial regions and slower ones in the bulk of the grains.

Finally in glassy materials the potential of the β-NMR relaxation technique to probe the local disorder was demonstrated. A systematic comparison of glassy and crystalline modifications of ion conductors covered lithium aluminosilicates where higher diffusion jump rates showed up in the glasses.

9.9 Appendix

In the following we list the full expressions for the dependence of the different NMR relaxation rates on the spectral densities described in Sect. 9.2 in a more qualitative way. A quantitative description includes a linear combination of spectral density functions $J^{(q)}$ which result in transitions of spin pairs, where the combined angular momentum changes by $q\hbar$, and thus involve contributions at ω_L and $2\omega_\mathrm{L}$. For pure dipolar interaction one gets for the spin-lattice relaxation rate [13]

$$\frac{1}{T_1} = \frac{3}{2}\gamma^4\hbar^2 I(I+1)\left[J^{(1)}(\omega_\mathrm{L}) + J^{(2)}(2\omega_\mathrm{L})\right] \tag{9.27}$$

and for the spin-spin relaxation rate

$$\frac{1}{T_2} = \frac{3}{8}\gamma^4\hbar^2 I(I+1)\left[J^{(0)}(0) + 10\,J^{(1)}(\omega_\mathrm{L}) + J^{(2)}(2\omega_\mathrm{L})\right] \quad . \tag{9.28}$$

The different contributions $J^{(0)}(\omega)$, $J^{(1)}(\omega)$ and $J^{(2)}(\omega)$ to the spectral density stem from the partitioning of the Hamiltonian to contributions which do not change the overall magnetization and those which cause a single or twofold spin flip. The spectral densities $J^{(q)}(\omega)$ $(q = 0, 1, 2)$ are calculated from the corresponding correlation functions $G^{(q)}(t)$ via a Fourier transform

$$J^{(q)}(\omega) = \int_{-\infty}^{\infty} G^{(q)}(t)\,\mathrm{e}^{\mathrm{i}\omega t}\,\mathrm{d}t \quad . \tag{9.29}$$

For powder samples the relation $J^{(0)}(\omega) : J^{(1)}(\omega) : J^{(2)}(\omega) = 6 : 1 : 4$ holds.

For the spin-lattice relaxation rate in the rotating reference frame the full expression is [15]

$$\frac{1}{T_{1\rho}} = \frac{3}{8}\gamma^4\hbar^2 I(I+1)\left[J^{(0)}(2\omega_1) + 10\,J^{(1)}(\omega_\mathrm{L}) + J^{(2)}(2\omega_\mathrm{L})\right] \tag{9.30}$$

where ω_1 denotes the Larmor frequency in the locking field B_1.

For β-NMR measurements we have to treat the case of highly diluted spins I interacting with a reservoir of spins S. For the longitudinal relaxation time one gets [13, 17]

$$\frac{1}{T_1} = \gamma_I^2\gamma_S^2\hbar^2 S(S+1)\left[\frac{1}{12}J^{(0)}(\omega_I - \omega_S) + \frac{3}{2}J^{(1)}(\omega_I) + \frac{3}{4}J^{(2)}(\omega_I + \omega_S)\right] \tag{9.31}$$

where ω_I and ω_S are the Larmor frequency of the spin I and S, respectively (see also Sect. 9.7.1). In case of quadrupolar interaction analogous results are obtained for NMR and β-NMR relaxation [13, 15, 39, 116].

Notation

a	unit cell dimension in x-direction
$a(r_{ik})$	coupling constant
a_β	β-asymmetry
A	asymmetry coefficient of a β-decay
A_f	fraction of motionally narrowed signal
A_p	pulse sequence parameter
b	unit cell dimension in y-direction
B_0	static magnetic induction ('field')
B_1	alternating magnetic induction ('field')
B_eff	effective magnetic induction ('field') in the rotating frame
c	unit cell dimension in z-direction
E_A	activation energy
$E_\mathrm{NMR}^\mathrm{lT}$, $E_\mathrm{NMR}^\mathrm{hT}$	activation energy from low-T, high-T side of T_1^{-1} peak
f	dipolar polarization
G	correlation function
$\hbar$	Planck constant divided by 2π
I	nuclear spin
J, $J^{(q)}$	spectral density function (angular momentum change $q\hbar$)
k_B	Boltzmann constant
m	power of distance dependence of coupling constant
M, M_0	magnetization (equilibrium value)
M_x, M_y, M_z	magnetization components in the laboratory frame
$M_{x'}$, $M_{y'}$, $M_{z'}$	magnetization components in the rotating frame
M_ρ	magnetization in the rotating frame
N	number density
P	nuclear polarization
P_hom, P_inh	homogeneously, inhomogeneously averaged nuclear polarization
r	distance
t	time
t_p	duration of a pulse
T	temperature
T_1	spin-lattice relaxation time in the laboratory frame
$T_{1\rho}$	spin-lattice relaxation time in the rotating frame
$T_{1\rho}$	spin-lattice relaxation time in the pulsed rotating frame
T_1inh, T_1hom	inhomogeneous, homogeneous spin-lattice relaxation time
T_2	spin-spin relaxation time
v/c	velocity of β-particle in units of light velocity
W	emission probability of β-particles
Z_N, Z_S	counting rates in counter 'North','South'
α	exponent for frequency dependence
β	exponent in stretched exponential
γ	magnetogyric ratio

$\Delta\nu_{\mathrm{R}}$	NMR linewidth of the rigid lattice
θ	angle between β-emission and nuclear polarization direction
θ_{p}	tilt angle of magnetization
τ	mean residence time between successive jumps
τ_{e}	time interval in magnetization recovery experiment
τ_{SAE}	correlation time obtained from spin-alignment echo NMR measurements
τ_β	mean lifetime of β-radioactive nuclide
τ_{c}	correlation time
ω	angular frequency
$\omega_{\mathrm{L}} = 2\pi\nu_{\mathrm{L}}$	Larmor frequency

References

1. *Materials Interfaces - Atomic-Level Structure and Properties*, ed by D. Wolf, S. Yip (Chapman & Hall, London 1992)
2. *Graphite Intercalation Compounds I, Structure and Dynamics*, Springer Series in Materials Science, vol 14, ed by H. Zabel, S.A. Solin (Springer, Berlin Heidelberg New York 1990)
3. *Graphite Intercalation Compounds II, Transport and Electronic Properties*, Springer Series in Materials Science, 14, ed by H. Zabel, S.A. Solin (Springer, Berlin Heidelberg New York 1992)
4. H. Gleiter: Progress in Materials Science **33**, 223 (1989)
5. R.W. Siegel: Nanophase Materials. In: *Encyclopedia of Applied Physics*, vol 11, ed by G.L. Trigg, E.H. Immergut, E.S. Vera, W. Greulich (VCH, New York 1994) pp 173–200
6. A. Feltz: *Amorphous Inorganic Materials and Glasses* (VCH, Weinheim 1993)
7. R. Zallen: *The Physics of Amorphous Solids* (Wiley, New York 1983)
8. M.D. Ingram: Phys. Chem. Glasses **28**, 215 (1987)
9. P. Heitjans, S. Indris: J. Phys.: Condens. Matter **15**, R1257 (2003)
10. G. Schatz, A. Weidinger: *Nuclear Condensed Matter Physics: Nuclear Methods and Applications* (Wiley, Chicester 1996)
11. P. Heitjans: Solid State Ionics **18/19**, 50 (1986)
12. H. Rickert: *Electrochemistry of Solids - An Introduction* (Springer, Berlin 1982)
13. A. Abragam: *The Principles of Nuclear Magnetism* (Clarendon, Oxford 1961)
14. C.P. Slichter: *Principles of Magnetic Resonance* (Springer, Berlin Heidelberg New York 1989)
15. A.R. Allnatt, A.B. Lidiard: *Atomic Transport in Solids* (Cambridge Univ. Press, Cambridge 1993)
16. N. Bloembergen, E.M. Purcell, R.V. Pound: Phys. Rev. **73**, 679 (1948)
17. P. Heitjans, A. Körblein, H. Ackermann, D. Dubbers, F. Fujara, H.-J. Stöckmann: J. Phys. F: Met. Phys. **15**, 41 (1985)
18. R. Messer, A. Seeger, K. Zick: Z. Metallkunde **80**, 299 (1989)
19. A. Schirmer, P. Heitjans. In: *XXVIIIth Congress Ampere on Magnetic Resonance and Related Phenomena*, ed by M.E. Smith, J.H. Strange (University of Kent, Canterbury 1996) p 416

20. A. Schirmer, P. Heitjans, G. Majer, A. Seeger: Defect Diffus. Forum **143-147**, 1317 (1997)
21. M. Mali, J. Roos, M. Sonderegger, D. Brinkmann, P. Heitjans: J. Phys. F: Met. Phys. **18**, 403 (1988)
22. R. Bertani, M. Mali, J. Roos, D. Brinkmann: J. Phys.: Condens. Matter **2**, 7911 (1990)
23. D.M. Fischer, P. Duwe, S. Indris, P. Heitjans: Solid State Nucl. Magn. Reson. **26**, 74 (2004)
24. C.A. Sholl: J. Phys. C: Solid State Phys. **14**, 447 (1981)
25. J.L. Bjorkstam, M. Villa: Magn. Res. Rev. **6**, 1 (1980)
26. E. Goebel, W. Müller-Warmuth, H. Olyschläger, H. Dutz: J. Magn. Reson. **36** 371 (1979)
27. D. Knödler, P. Pendzig, W. Dieterich: Solid State Ionics **86–88**, 29 (1996)
28. K.L. Ngai, O. Kanert: Solid State Ionics **53-56**, 936 (1992)
29. K. Funke: Progr. Solid State Chem. **22**, 111 (1993)
30. M. Meyer, P. Maass, A. Bunde: Phys. Rev. Lett. **71**, 573 (1993)
31. H.-J. Stöckmann: J. Phys.: Condens. Matter **1**, 5101 (1989)
32. P. Borgs, K.W. Kehr, P. Heitjans: Phys. Rev. B **52**, 6668 (1995)
33. R.R. Ernst, G. Bodenhausen, A. Wokaun: *Principles of Nuclear Magnetic Resonance in One and Two Dimensions* (Clarendon Press, Oxford 1987)
34. M. Mehring: *High Resolution NMR Spectroscopy in Solids* (Springer, Berlin Heidelberg New York 1983)
35. *Solid State NMR I, III, IV*, ed by B. Blümich. In: *NMR Basic Principles and Progress* vol 30, 32, 33, ed by P. Diehl, E. Fluck, H. Günther, R. Kosfeld, J. Seelig (Springer, Berlin Heidelberg New York 1994)
36. E. Fukushima, R. Roeder: *Experimental Pulse NMR* (Addison Wesley, London 1981)
37. B.C. Gerstein, C.R. Dybowski: *Transient Techniques in NMR of Solids* (Academic, New York 1985)
38. R. Kimmich, E. Anoardo: Prog. Nucl. Magn. Reson. Spectrosc. **44**, 257 (2004)
39. H. Ackermann, P. Heitjans, H.-J. Stöckmann: β Emitters and Isomeric Nuclei as Probes in Condensed Matter. In: *Hyperfine Interactions of Radioactive Nuclei*, Topics in Current Physics, vol 31, ed by J. Christiansen (Springer, Berlin Heidelberg New York 1983) pp 291–361
40. H. Ackermann, N.T. Bagraev, R.T. Harley, J. Schneider. In: *Hyperfine Interaction of Defects in Semiconductors*, ed by G. Langouche (Elsevier, Amsterdam 1992) p 323
41. K. Sugimoto, A. Mizobuchi, K. Nakai, K. Matuda: J. Phys. Soc. Jpn. **21**, 213 (1966)
42. Y. Nojiri, B.I. Deutch: Phys. Rev. Lett. **51**, 180 (1983)
43. W. Faber, E. Jäger, B. Ittermann, H. Ackermann, P. Heitjans, H.-J. Stöckmann: Nucl. Instrum. Methods Phys. Res. B **16**, 439 (1986)
44. B. Ittermann, M. Füllgrabe, M. Heemeier, F. Kroll, F. Mai, K. Marbach, P. Meier, D. Peters, G. Welker, W. Geithner, S. Kappertz, S. Wilbert, P. Neugart, P. Lievens, U. Georg, M. Keim, and the ISOLDE Collaboration: Hyperfine Interact. **129**, 423 (2000)
45. R.F. Kiefl, W.A. MacFarlane, G.D. Morris, P. Amaudruz, D. Arsenau, H. Azumi, R. Baartman, T.R. Beals, J. Behr, C. Bommas, J.H. Brewer, K.H. Chow, E. Dumont, S.R. Dunsiger, S. Daviel, L. Greene, A. Hatakeyama

R.H. Heffner, Y. Hirayama, B. Hitti, S.R. Kreitzmann, C.D.P. Levy, R.I. Miller, M. Olivio, R. Poutissou: Physica B **326**, 189 (2003)
46. T.K. McNab, J.D. Perez, R.E. McDonald: Phys. Rev. B **18**, 92 (1978)
47. J.D. Perez, R.E. McDonald, T.K. McNab: Phys. Rev. B **19**, 163 (1979)
48. B. Ittermann, H. Ackermann, H.-J. Stöckmann, K.-H. Ergezinger, M. Heemeier, F. Kroll, F. Mai, K. Marbach, D. Peters, G. Sulzer: Phys. Rev. Lett. **77**, 4784 (1996)
49. M. Füllgrabe, B. Ittermann, H.-J. Stöckmann, F. Kroll, D. Peters, H. Ackermann: Phys. Rev. B **64**, 224302 (2001)
50. B. Ittermann, D. Peters, M. Füllgrabe, F. Kroll, H. Ackermann, H.-J. Stöckmann: Physica B **308–310**, 236 (2001)
51. H.D. Ebinger, H. Arnolds, C. Polenz, B. Polivka, W. Preyß, R. Veith, D. Fick, H.J. Jänsch: Surf. Sci. **412/413**, 586 (1998)
52. C. Bromberger, H.J. Jänsch, O. Kühlert, R. Schillinger, D. Fick: Phys. Rev. B **69**, 245424 (2004).
53. P. Heitjans, W. Faber, A. Schirmer: J. Non-Cryst. Solids **131-133**, 1053 (1991)
54. M.S. Wittingham: Prog. Solid State Chem. **12**, 41 (1978)
55. A. Schirmer, P. Heitjans, W. Faber, J.E. Fischer: Synth. Met. **34**, 589 (1989)
56. A. Schirmer, P. Heitjans, W. Faber, J.E. Fischer: Mater. Sci. Forum **91-93**, 589 (1992)
57. P. Freiländer, P. Heitjans, H. Ackermann, B. Bader, G. Kiese, A. Schirmer, H.-J. Stöckmann, C. Van der Marel, A. Magerl, H. Zabel: Z. Phys. Chem. N. F. **151**, 93 (1987)
58. J. Corish, F. Jugie, D.A. Morton-Blake, M. Leslie, F. Bénière: Phys. Rev. B **41**, 10870 (1990)
59. A. Schirmer, P. Heitjans: Z. Naturforsch. **50a**, 643 (1995)
60. S. Sinha, D. W. Murphy: Solid State Ionics **20**, 81 (1986)
61. R. Schöllhorn, A. Payer: Angew. Chem. **97**, 57 (1985)
62. W. Küchler, P. Heitjans, A. Payer, R. Schöllhorn: Solid State Ionics **70/71**, 434 (1994)
63. R.L. Kleinberg, B.G. Silbernagel: Solid State Comm. **36**, 345 (1980)
64. H.W. Spiess: J. Chem. Phys. **72**, 6755 (1980)
65. R. Böhmer: J. Magn. Reson. **147**, 78 (2000)
66. M. Wilkening, P. Heitjans: Defect Diffus. Forum **237-240**, 1182 (2005)
67. T. Bredow, P. Heitjans, M. Wilkening: Phys. Rev. B **70**, 115111 (2004)
68. B. Bader, P. Heitjans, H.-J. Stöckmann, H. Ackermann, W. Buttler, P. Freiländer, G. Kiese, C. van der Marel, A. Schirmer: J. Phys.: Condens. Matter **4**, 4779 (1992)
69. W. Puin, S. Rodewald, R. Ramlau, P. Heitjans, J. Maier: Solid State Ionics **131**, 159 (2000)
70. R.S. Averbach, H. Hahn, H.J. Höfler, J.L. Logas, T.C. Shen: Mat. Res. Soc. Symp. Proc. **153**, 3 (1989)
71. S. Indris, P. Heitjans: Mater. Sci. Forum **343-346**, 417 (2000)
72. S. Indris, D. Bork, P. Heitjans: J. Mater. Synth. Process. **8**, 245 (2000)
73. P. Heitjans, S. Indris. In: *Synthesis, Functional Properties and Applications of Nanostructures*, MRS symposium proceedings, vol 676, ed by H.W. Hahn, D.L. Feldheim, C.P. Kubiak, R. Tannenbaum, R.W. Siegel (Materials Research Society, Pittsburgh 2002) pp 6.6.1–6.6.10
74. R. Van Steenwinkel: Z. Naturforsch. **29a**, 278 (1974)

75. W. Puin, P. Heitjans, W. Dickenscheidt, H. Gleiter. In: *Defects in Insulating Materials*, ed by O. Kanert, J.M. Spaeth (World Scientific, Singapore 1993) pp 137–139
76. W. Puin, P. Heitjans: Nanostructured Materials **6**, 885 (1995)
77. W. Dickenscheid, R. Birringer, R. Strauß, H. Gleiter, O. Kanert, B. Michel, B. Günther: Solid State Comm. **79**, 683 (1991)
78. P. Heitjans, S. Indris: J. Mater. Sci. **39**, 5091 (2004)
79. D. Bork, P. Heitjans: J. Phys. Chem. B **102**, 7303 (1998)
80. D. Bork, P. Heitjans: J. Phys. Chem. B **105**, 9162 (2001)
81. M. Wilkening, D. Bork, S. Indris, P. Heitjans: Phys. Chem. Chem. Phys. **4**, 3246 (2002)
82. W.-K. Rhim, D.P. Burum, D.D. Ellemann: J. Chem. Phys. **68**, 692 (1978)
83. D. Bork, P. Heitjans. In: *XXVIIIth Congress Ampere on Magnetic Resonance and Related Phenomena*, ed by M.E. Smith, J.H. Strange (University of Kent, Canterbury 1996) p 418
84. J.R. Hendrickson, P.J. Bray: J. Magn. Reson. **9**, 341 (1973)
85. R. Winter, P. Heitjans: J. Phys. Chem. B **105**, 6108 (2001)
86. G. Balzer-Jöllenbeck, O. Kanert, H. Jain, K.L. Ngai: Phys. Rev. B **39**, 6071 (1989)
87. W. Franke, P. Heitjans: Ber. Bunsenges. Phys. Chem. **96**, 1674 (1992)
88. R. Winter, K. Siegmund, P. Heitjans: J. Non-Cryst. Solids **212**, 215 (1997)
89. A. Schirmer, P. Heitjans, H. Ackermann, B. Bader, P. Freiländer, H.-J. Stöckmann: Solid State Ionics **28–30**, 717 (1988)
90. A. Schirmer, P. Heitjans, B. Bader, P. Freiländer, H.-J. Stöckmann, H. Ackermann: J. Phys.: Condens. Matter **3**, 4323 (1991)
91. A. Schirmer, P. Heitjans. In: *The Physics of Non-Crystalline Solids*, ed by D. Pye, W.C. LaCourse, H.J. Stevens (Taylor & Francis, London 1992) p 59
92. A. Pradel, G. Taillades, C. Cramer, M. Ribes: Solid State Ionics **105**, 139 (1998)
93. S. Indris, P. Heitjans, H. E. Roman, A. Bunde: Phys. Rev. Lett. **84**, 2889 (2000)
94. S. Indris, P. Heitjans, H. E. Roman, A. Bunde: Defect Diffus. Forum **194-199**, 935 (2001)
95. M. Ulrich, A. Bunde, S. Indris, P. Heitjans: Phys. Chem. Chem. Phys. **6**, 3680 (2004)
96. S. Indris, P. Heitjans, M. Ulrich, A. Bunde: Z. Phys. Chem. **219**, 89 (2005)
97. N.J. Dudney: Ann. Rev. Mater. Sci. **19**, 113 (1989)
98. J. Maier: Prog. Solid St. Chem. **23**, 171 (1995)
99. J. Maier: Solid State Ionics **154-155**, 291 (2002); *ibid.* **157**, 327 (2003)
100. J. Maier: *Physical Chemistry of Materials: Ions and Electrons in Solids* (Wiley, Chichester 2004)
101. J.-M. Debierre, P. Knauth, G. Albinet: Appl. Phys. Lett. **71**, 1335 (1997)
102. A. Bunde, W. Dieterich, H.E. Roman: Phys. Rev. Lett. **55**, 5 (1985)
103. S. Indris, P. Heitjans: J. Non-Cryst. Solids **307–310**, 555 (2002)
104. M. Wilkening, S. Indris, P. Heitjans: Phys. Chem. Chem. Phys. **5**, 2225 (2003)
105. P. Heitjans, B. Bader, H.-J. Stöckmann, K. Dörr, G. Kiese, H. Ackermann, P. Freiländer, W. Müller-Warmuth, K. Meise-Gresch: Hyperfine Interact. **15/16**, 597 (1983)
106. H.-J. Stöckmann, P. Heitjans: J. Non-Cyst. Solids **66**, 501 (1984)

107. W. Faber, P. Heitjans, A. Schirmer. In: *Dynamics of Disordered Materials*, Springer Proceedings in Physics, vol 37, ed by D. Richter, A.J. Dianoux, W. Petry, J. Teixeira (Springer, Berlin Heidelberg New York 1989) p 69
108. W. Pannhorst, R. Haug, E. Rodek, K. Stetter: J. Non-Cryst. Solids **131-133**, 488 (1991)
109. P. Maass, A. Bunde, M.D. Ingram: Phys. Rev. Lett. **68**, 3064 (1992)
110. W. Dieterich, D. Knödler, P. Pendzig: J. Non-Cryst. Solids **172-174**, 1237 (1994)
111. T. Wichmann, K.G. Wang, K.W. Kehr: J. Phys. A: Math. Gen. **27**, L263 (1994)
112. B. Munro, M. Schrader, P. Heitjans: Ber. Bunsenges. Phys. Chem. **96**, 1718 (1992)
113. K. Ngai: J. Chem. Phys. **98**, 6424 (1993)
114. R. Goldstein: Diploma Thesis, Universität Hannover (2001)
115. F. Qi, C. Rier, R. Böhmer, W. Franke, P. Heitjans: Phys. Rev. B **72**, 104301 (2005)
116. A. Körblein, P. Heitjans, H.-J. Stöckmann, F. Fujara, H. Ackermann, W. Buttler, K. Dörr, H. Grupp: J. Phys. F: Met. Phys. **15**, 561 (1985)